이학박사학위논문

금속 나노구조 안에서 일어나는 테라헤르츠 갭 플라즈몬과 유전체의 상호작용 연구

Strong coupling of dielectrics with terahertz gap plasmons within metallic nano-slots

2018년 2월

서울대학교 대학원
물리천문학부
정지윤

금속 나노구조 안에서 일어나는 테라헤르츠 갭 플라즈몬과 유전체의 상호작용 연구

Strong coupling of dielectrics with terahertz gap plasmons within metallic nano-slots

지도교수 김 대 식

이 논문을 이학박사 학위논문으로 제출함

2018년 2월

서울대학교 대학원

물리천문학부

정지윤

정지윤의 박사 학위논문을 인준함

2018년 2월

위 원 장	전 헌 수	(인)
부위원장	김 대 식	(인)
위 원	박 건 식	(인)
위 원	홍 승 훈	(인)
위 원	박 형 렬	(인)

Abstract

In this work a 'real metal regime' of metallic nanostructures in terahertz frequencies, where most noble metals are treated as perfect electric conductors, is discussed. With an aid from gap plasmon modes, that is, coupling of surface plasmons from the two metal sides forming a gap, large amount of terahertz electric field can enter the metal with electric permittivity of 10^6 when the gap is smaller than 100 nm. A method for high-throughput fabrication of such gaps is first presented, and then peculiar optical responses – anomalous resonance shifts and a large Ohmic absorption – are experimentally and theoretically realized. Also, wet etching of a gap spacer within a 5 nm gap is demonstrated, enabling aqueous nano-optic experiments below 10 nm scale. This comprehensive study on terahertz gap plasmon and nanogaps is expected to greatly benefit convergence of chemistry or bio-chemistry with nano-optics, especially in sub-10 nm regime.

Keywords : Terahertz nano-gaps, Gap plasmons, Metamaterial absorber

Student Number : 2014-30106

Table of Contents

List of Figures

Chapter 1

Introduction

Terahertz (THz = 10^{12} Hz) is an intermediate frequency between optics (100 THz) and electronics (1 GHz), where various intriguing phenomena such as intermolecular interactions[1, 2, 3], quasiparticles[4], and superconducting gaps[5, 6, 7] lie. Energy scale associated with the frequency range is *meV*, which is far below most of molecular electronic excitation energies. Such low photon energy is useful for investigating biological systems [8, 9] and other non-destructive inspection applications[10, 11].

Meanwhile, noble metals such as gold and silver, whose plasma frequencies are orders of magnitude larger than the frequencies of interest (10^4 THz) show more electronic response than optic response at THz frequencies[12, 13], and therefore are considered as perfect electric conductor in most of practical situations. While such properties are less advantageous in plas-

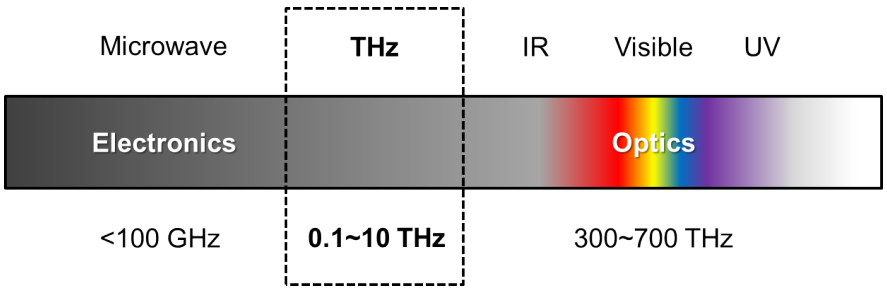

Figure 1.1: Terahertz radiation, lying between electronics and optics.

monic applications since perfect metals cannot support surface plasmons, the extremely high refractive index at terahertz frequencies ($500 + 600i$ at 1 THz) enables extremely high degree of electromagnetic confinement, and accordingly high electric field enhancement under appropriate design of the metallic gap structures. Therefore an exclusive funneling of electromagnetic fields into nanogaps have been successfully demonstrated, and nearly perfect transmission has been demonstrated through nanogaps with widths as small as 200 nanometers [14, 15].

Yet, as sub-10 nm terahertz nanostructures are realized via recent advances in nanofabrication technologies, such perfect transmission is no longer demonstrated. In fact, an extremely dense nanogap array barely transmits more than 60% of incident field when the gap width is smaller than 10 nm (Figure 1.2, images from [14, 15, 16]). This implies that a new regime of terahertz nano-optics is reached, where noble metals can no more be considered 'perfect'. In this work, we investigate such 'real metal regime' of terahertz nanostructures. First we demonstrate wafer scale, high-throughput fabrication of sub-10 nm metallic nanostructures. Then we investigate the physical origin of the real metal effects emerging in such gaps, which we contribute to gap plasmon modes formed inside the gap. Lastly we show how the gap plasmon mode respond to changes in the dielectric environments inside the gap, and discuss the applicability of such system.

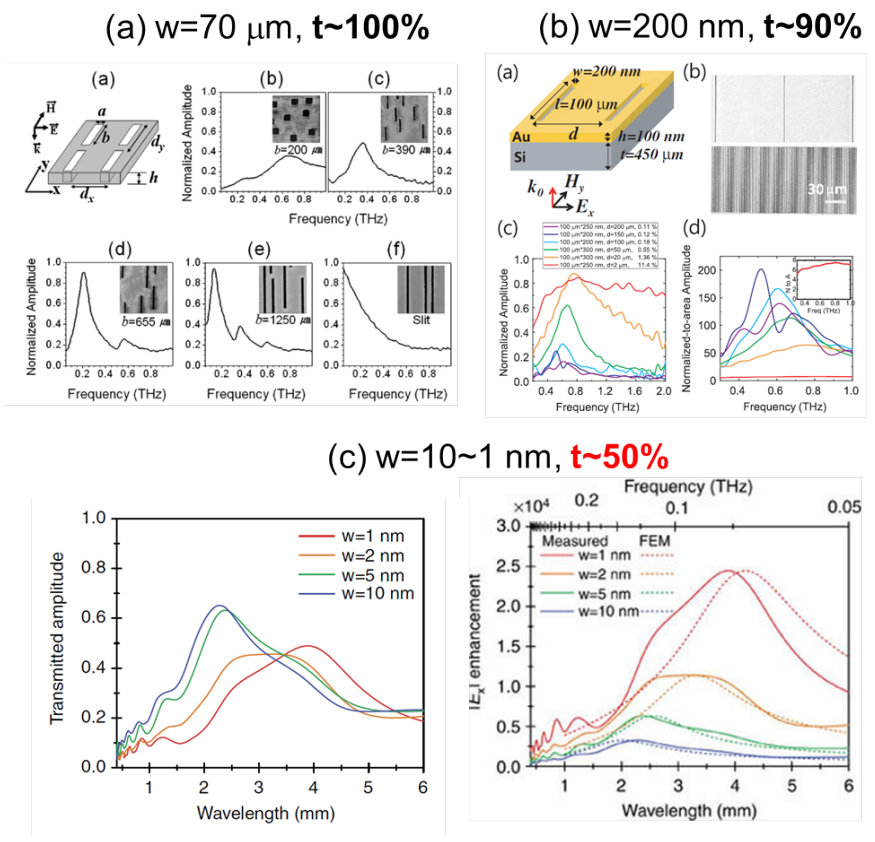

Figure 1.2: Evolution of terahertz slot antennas and their transmissions. (a) 100% transmission through random arrays of 70 μm gaps. (b) 90% transmission through 200 nm gap arrays. (c) Transmission through sub-10 nm gaps, smaller than 70% even with extremely high density.

1.1 Terahertz time-domain spectroscopy

Among many ways to generate terahertz radiation such as a quantum cascade laser [17, 18], a free electron laser [19, 20] and a synchrotron source [21, 22], etc., a pulsed source generated from optical rectification or an antenna is the most commonly used. When such pulses are used, a time-domain measurement technique is useful. Since such technique directly measures the electric field of a pulse, and not the power, amplitude and phase information can simultaneously obtained. This is advantageous in characterizing optical properties of a target material since real and imaginary part of refractive index can directly be determined without use of Kramers-Kronig relations.

Terahertz time-domain spectroscopy used in this study utilizes picosecond, single-cycle pulses emitting from semiconductors illuminated by femtosecond optical pulses[23, 24]. A brief schematic is illustrated in Figure 1.3. First, a train of femtosecond pulses from a Ti:sapphire cavity is split into pump and probe beams. The pump beam optically excites a photoconductive antenna, generating the THz pulses via built-in field inside a semiconductor or photo-Dember effect. In the home-made setup used in this study, a DC-biased low-temperature grown gallium arsenide (LT-GaAs) is used as the emitter for simple transmission and reflection measurements[25]. When high power optical pulses from regenerative amplifier are used, tilted-front rectification from lithium niobate generates THz pulses with peak amplitude of $\sim$ 1 MV/cm[26, 27]. Such intense THz pulses are used for observation of nonlinear phenomena inside the nanogaps. In our experiments, a pump laser

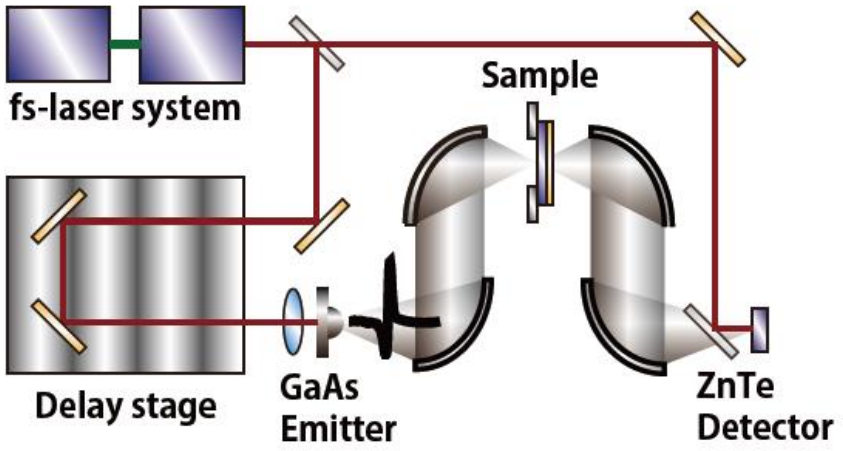

Figure 1.3: A schematic of a typical terahertz time-domain spectroscopy setup.

Coherent Verdi V5 and a Ti:sapphire cavity *Coherent Mira900* are used to generate 80 MHz pulse train with center frequency 805 nm and pulse width 160 fs. The output power is 500 mW and the resulting peak THz electric field amplitude is 30 V/cm. For intense THz experiments a regenerative amplifier system from *SpectraPhysics* is used as the pump pulse source with repetition rate of 1 KHz (*MaiTai, Empower, Spitfire Ace*). The output power was 5.6 W and resulting peak THz electric field was 460 KV/cm.

The instantaneous value of transmitted or reflected THz waves from the sample is measured via electro-optic (EO) effect from zinc telluride or gallium phosphide crystal[28, 29]. Being a reciprocal process of optical rectification, the EO process induces a birefringence inside an EO crystal upon irradiation of THz electric field, which in turn changes polarization of the probe beam passing through the EO crystal. The polarization change is ana-

lyzed with balanced detection method. The observed polarization change is later converted to THz field amplitude via following formula,

$$\Gamma = (\pi d n_0^3 \gamma_{41} E)/\lambda \times \sqrt{(1+3\sin 2\phi)} \tag{1.1}$$

where Γ is the phase delay between the two optical axes, d is thickness of the crystal, n_0 is refractive index of the crystal, $_{41}$ is the EO coefficient, λ is wavelength, and E is the instantaneous amplitude of the THz electric field.

The observed real-time electric field amplitude is converted to frequency domain data via finite Fourier transform. Figure 1.4 shows an example of measured and Fourier-transformed signal. Since most samples we use are fabricated on top of a dielectric substrate, there are multiple reflections coming from reflections from the edges of the substrate which makes spurious Fabry-Perot type oscillations in the frequency-domain spectrum. The oscillation does not disappear even after normalization with respect to bare substrate since there exists a phase difference between multiple reflections coming from the bare substrate and the sample. We can take advantage of the single-cycled nature of the THz source to selectively remove the multiple reflections by Fourier-transforming only the first transmitted (or reflected) pulse. For example, a 500 micron-thick silicon substrate ($n_{Si} = 3.4$) makes multiple reflections every $2 \times 500\mu m \times 3.4/(3 \times 10^8 m/s) = 11ps$. Then we can use only the first 10 ps for finite Fourier transform, obtaining Fabry-Perot free spectrum yet with limited spectral resolution of $1/11ps =$ 0.09THz. Since our sample is a relatively broad resonator with bandwidth larger than 0.2 THz, the resolution limit does not affect our measurement.

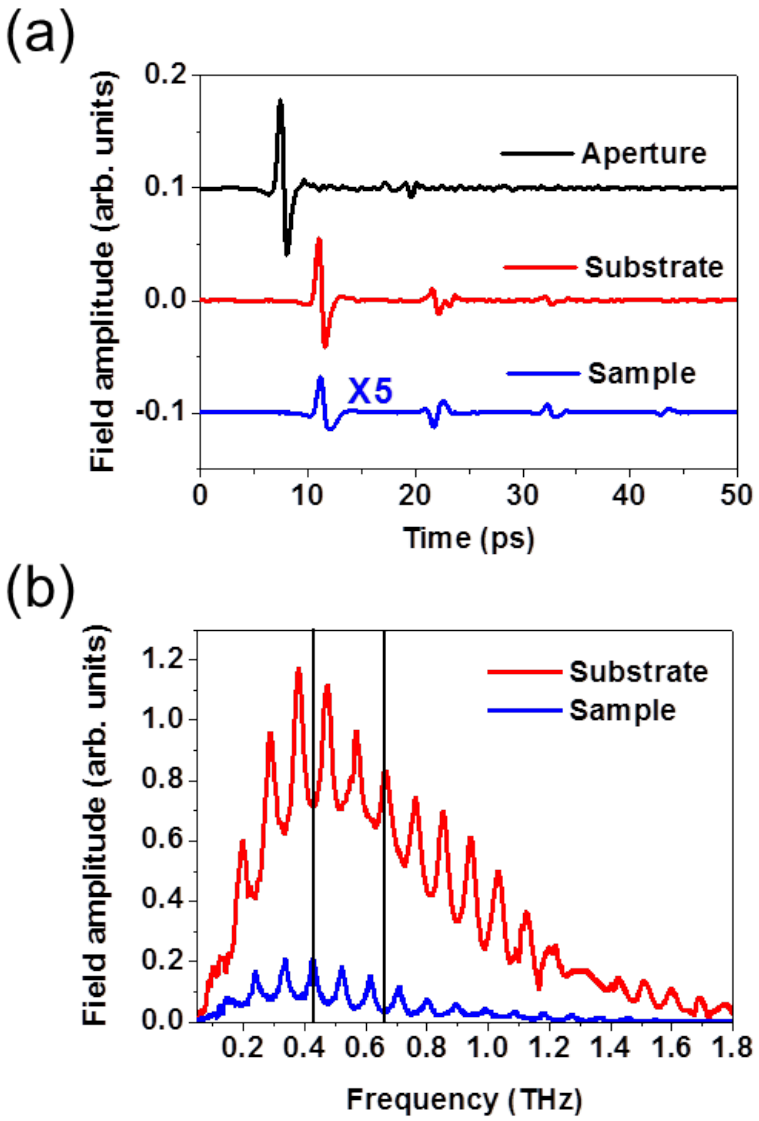

Figure 1.4: Signals obtained from THz-TDS. (a) Time traces of transmitted waves through a bare aperture, a silicon substrate, and a nano-slit array sample. (b) Fourier-transformed spectra of the substrate and the sample. Peaks and valleys in the black line show that there is a phase difference of π between multiple reflections from the substrate and the sample.

1.2 Field enhancement in terahertz slot antennas

Among many structures designed for terahertz field enhancement such as slits[30, 31], bowties[32, 33], and tips[34, 35], slot antennas are one of the most extensively studied[36, 37, 38, 14, 39]. The structure is easy to analyze since electric field distribution inside the gap follows that of a rectangular waveguide, and can safely be approximated to be in a single TE_{10} mode when the gap width is sufficiently small. Also, the gap is capable of confining electromagnetic field within a depth equivalent to its gap, enabling selective detection of target system inside the gap, or on top of it as well. Lastly, the structure benefits from absence of background signal under transmission geometry. This means that transmitted field solely comes from the gap and therefore it is possible to experimentally determine the field enhancement factor without access to nonlinear phenomena[32]. Such advantages have enabled numerous applications in terahertz nano-optics, including metal-insulator transition-based switching device[40, 41, 42], molecular absorption enhancement[43, 44], detection of nanoparticles[45, 46] and non-destructive probing of surface carrier dynamics[47].

As briefly mentioned above, exclusive funneling of electromagnetic waves through slot antennas creates direct link between far field transmission and the near field enhancement at the gap using a diffraction theory referred to as Kirchhoff integral formalism[48]. A brief schematic is shown in Figure 1.5. For a wave passing through an aperture, electric field at an

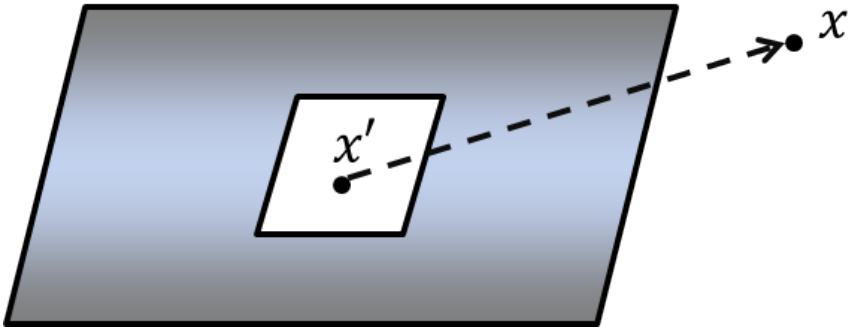

Figure 1.5: Schematic of Kirchhoff integral formalism, where electric field inside an aperture (x') is integrated to give far field electric field at a detection point x.

observation point x can be written as:

$$\vec{E}(r) = \frac{ie^{ikr}}{2\pi r}\vec{k} \times \int \hat{n} \times \vec{E}(r')e^{i\vec{k}\times\vec{r}'}da' \tag{1.2}$$

For an x-polarized electromagnetic wave propagating in z direction, above formula simplifies to:

$$E_{far} = \frac{e^{ikr}}{i\lambda r}\int E_{near}dx'dy' = \frac{e^{ikr}}{i\lambda r} < E_{near} > A \tag{1.3}$$

Here bracket means averaging over area of the aperture. Therefore normalized transmitted amplitude, that is, transmitted amplitude through a slot antenna divided by that through a bare substrate, can be expressed as:

$$\frac{E_{far,slot}}{E_{far,substrate}} = \frac{E_{near,slot}}{E_{near,substrate}} \times \frac{A_{slot}}{A_{substrate}} \tag{1.4}$$

So the near field enhancement in the slot is simply normalized transmitted

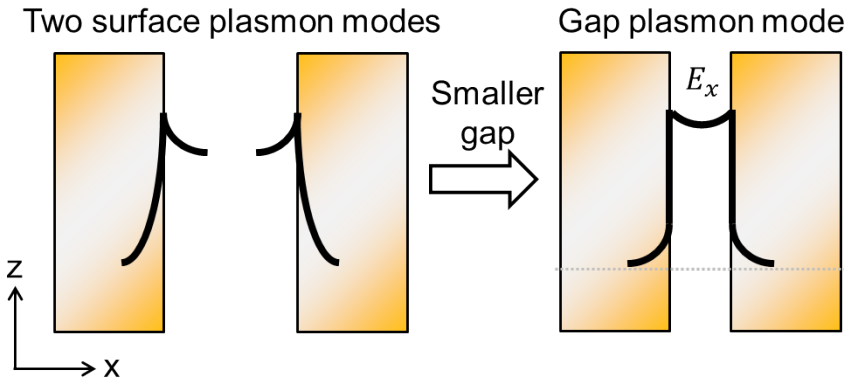

Figure 1.6: Schematic of gap plasmon emerging in a narrow gap.

amplitude divided by the gap coverage ratio, $\frac{A_{slot}}{A_{substrate}}$.

One thing to note is that this formalism is based on a point detection, while in experimental setup diffracted THz waves from the sample is focused with a parabolic mirror. The inferred near field value from the Kirchhoff integral formalism might therefore deviate significantly from the real value if the sample has a very high scattering angle and the numerical aperture of parabolic mirror in front of the detector is high. In this experiment all the nanogap samples are arrays with deep sub-wavelength periods, such that most of the transmission through the gaps propagates straight. Also, relatively low numerical aperture of the parabolic mirror (NA=0.25) ensures the validity of the Kirchhoff integral formalism.

1.3 Gap plasmons in visible and terahertz frequencies

While a metal-dielectric interface can support surface plasmon under momentum matching, a metal-insulator-metal (MIM) geometry can support gap plasmon modes via coupling between the two metal layers. Gap plasmon modes are essentially a symmetric coupling of two adjacent surface plasmon modes, as depicted in Figure 1.6. Dispersion relation of the gap plasmon can be deduced from calculating transverse magnetic (TM) mode in parallel plate waveguide geometry[49]. First, electromagnetic fields at metal layer I can be written as:

$$H_y = Ae^{i\beta z}e^{-k_1 x} \tag{1.5}$$

$$E_z = iA\frac{k_1}{\omega\varepsilon_0\varepsilon_1}e^{i\beta z}e^{-k_1 x} \tag{1.6}$$

$$E_x = -A\frac{\beta}{\omega\varepsilon_0\varepsilon_1}e^{i\beta z}e^{-k_1 x} \tag{1.7}$$

At metal layer III, the fields are written as:

$$H_y = Be^{i\beta z}e^{k_3 x} \tag{1.8}$$

$$E_z = -iB\frac{k_3}{\omega\varepsilon_0\varepsilon_3}e^{i\beta z}e^{k_3 x} \tag{1.9}$$

$$E_x = B\frac{\beta}{\omega\varepsilon_0\varepsilon_3}e^{i\beta z}e^{k_3 x} \tag{1.10}$$

Finally, the fields in the gap (region II) are expressed as:

$$H_y = Ce^{i\beta z}e^{k_2 x} + De^{i\beta z}e^{-k_2 x} \tag{1.11}$$

$$E_z = C\frac{-ik_2}{\omega\varepsilon_0\varepsilon_2}e^{i\beta z}e^{k_2 x} + D\frac{ik_2}{\omega\varepsilon_0\varepsilon_2}e^{i\beta z}e^{-k_2 x} \tag{1.12}$$

$$E_x = C\frac{\beta}{\omega\varepsilon_0\varepsilon_2}e^{i\beta z}e^{k_2 x} + D\frac{\beta}{\omega\varepsilon_0\varepsilon_2}e^{i\beta z}e^{-k_2 x} \tag{1.13}$$

In the special case of $\varepsilon_1 = \varepsilon_3$,$k_1 = k_3$ and $C = D$. Therefore, matching boundary conditions at each interface leads to an equation of the form:

$$\tanh k_2 a = -\frac{k_1\varepsilon_2}{k_2\varepsilon_1} \tag{1.14}$$

where wave equation should be fulfilled in both metal and dielectric region (i=1, 2 for metal, dielectric, respectively)

$$k_i^2 = \beta^2 - k_0^2\varepsilon_i \tag{1.15}$$

Figure 1.7 shows the gap plasmon dispersion relation. It shows that a large propagation constant can be obtained even in frequencies well below the surface plasmon frequency. For sufficiently small gaps, even terahertz waves can excite the gap plasmon modes. As a means to quantify the effect of gap plasmon, we try to express k_2 explicitly. For a deep sub-wavelength gap $\lambda >> a$, following approximation can be made for k_2,

$$k_2^2 = -1 - \frac{\sqrt{1 - 4k_0^2(\frac{w\varepsilon_1}{2\varepsilon 2})^2(\varepsilon_1 - \varepsilon_2)}}{2(\frac{w\varepsilon_1}{2\varepsilon 2})^2} \tag{1.16}$$

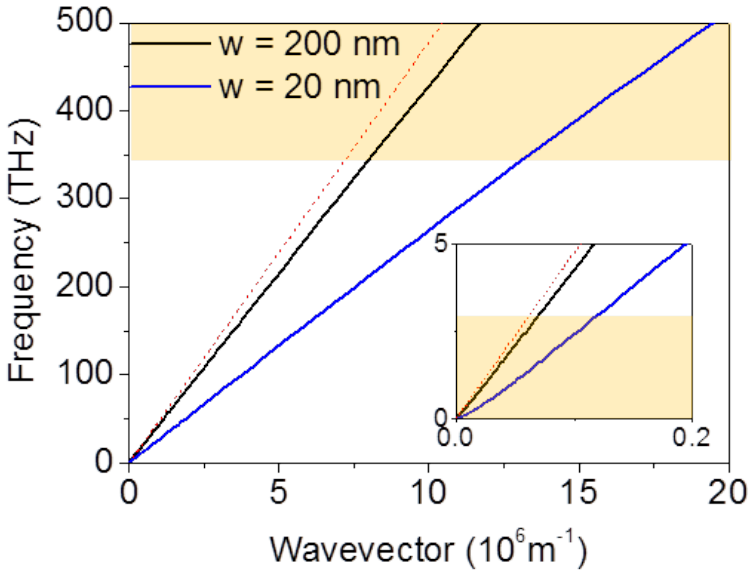

Figure 1.7: Dispersion relation of gap plasmon mode in a gold-air-gold gap geometry.

which can be further simplified in the limit $\varepsilon_1 >> \varepsilon_2$,

$$\frac{k_2^2}{k_0^2} = \frac{\sqrt{\varepsilon_2}}{\pi}\left(\frac{\lambda\varepsilon_2}{w\varepsilon_1}\right) \tag{1.17}$$

This relation provides a convenient means to quantify how predominant the gap plasmon is in a nanogap, with a dimensionless factor $\frac{\lambda\varepsilon_2}{w\varepsilon_1}$. It is clear that gap plasmon effect is stronger for higher permittivity contrast between the gap and the metal, and smaller gap size with respect to incident wavelength. For example, a 100 nm gap fabricated on a gold film show $\frac{k_1^2}{k_0^2} = 1$ at 1 THz; that is, effective permittivity increase caused by gap plasmon coupling is the same order as the original permittivity of the gap. This is due to a huge permittivity of metals in terahertz frequencies (10^6). In contrast, the same gap shows only 10% change in $\frac{k_1^2}{k_0^2}$ in infrared frequencies with wavelength 3 microns. While many researches reported on the effect of gap plasmon on optical properties of nanostructures[50, 51, 52, 53], the effect is much more dramatic in terahertz frequencies, and is essential to understand the phenomena quantitatively when working with sub-100 nm nanostructures.

As a last reminder, since the gap plasmon mode is stronger in geometries with smaller permittivity contrast between metal and gap material, it means that metal is 'less perfect' when it is under the influence of gap plasmon mode. By observing the gap plasmon effect therefore we are investigating the real metal regime of terahertz nano-optics. And since the gap plasmon is essentially a coupling between the gap and the metals, waves propagate much slower when the gap plasmon is present, that is, the effective refractive index of the gap becomes larger. The existence of gap plas-

mon therefore increases sensitivity of the waveguide to changes in dielectric environment of the gap.

Chapter 2

Fabricating gap plasmon-dominant terahertz nano-slots

2.1 Exfoliation-based method

For a terahertz nano-slot to be in a gap plasmon-dominant regime, as demonstrated in the previous section, it must have a sub-100 nm wide gap extending over lengths of over several hundreds of microns. Such requirement on high aspect ratio is technically very demanding for commonly used nanofabrication techniques such as focused ion beam (FIB) milling or electron beam lithography (EBL). Alternative techniques such as shadow mask evaporation partially succeeded in achieving high aspect ratio gaps, yet with limitations in accessible geometries and fabrication throughput[54, 55].

In 2013 X. Chen et al demonstrated that spacer based fabrication technique can overcome the limits of conventional nanofabrication tools[16]. The key idea is to define shapes of nanogaps with photolithography, and determine the gap size with deposition height of a dielectric layer. Figure 2.1 shows the overall procedure of the fabrication process. First a conventional photolithography and lift-off of metal layer defines the perimeter where the gap is to be formed. Then, to make gaps vertically aligned to the substrate in order for a convenient optic measurements, a dielectric layer is uniformly

coated around the patterned metal layer, both on top and on the sidewalls. Atomic layer deposition (ALD) is very well suited for this procedure since it is capable of conformal deposition of dielectrics with 1 nm precision[56]. Then another layer of metal is deposited without an adhesive layer to fill the trench and define the metal-insulator-metal gap at the edges of the pre-patterned metal layer. The overhanging excess metal layer can then be removed with an adhesive tape, since adhesion of the second deposited metal to the deposited dielectrics is weak.

This method breaks the resolution limit of conventional fabrication tools while enabling large patterns to be made in wafer-scale. Yet the fabrication procedure is difficult to follow and the throughput is relatively low. To selectively remove only the overhanging metal layer, and not the filling layer, it is crucial for the first patterned metal layer to have vertical sidewalls. Otherwise the second deposition will lead to connection of the filling layer and the overhanging layer, making it impossible to mechanically separate the two layers. The photolithography condition and evaporator system should therefore be very well calibrated in order to fabricate samples successfully. In addition, the fabricated sample might be vulnerable to mechanical agitation due to the weak adhesion.

2.2 Chemical etching-based method

To circumvent such issues for the spacer-based sample fabrication, J. Jeong et al., reported a way to mitigate the requirements while maintaining all the advantages of the spacer-based technique[57]. The key idea is to use

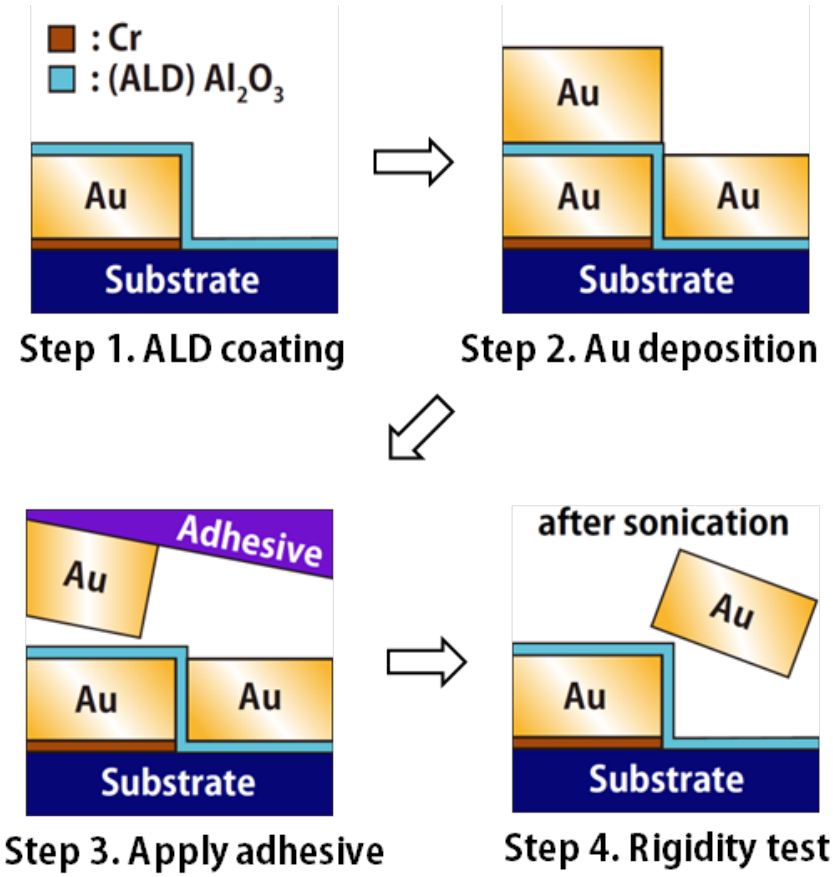

Figure 2.1: Spacer-based nanogap fabrication utilizing mechanical exfoliation for selective removal of excess metal layer. The second deposition of metal must be adhesion-free, leaving the sample vulnerable to mechanical agitations.

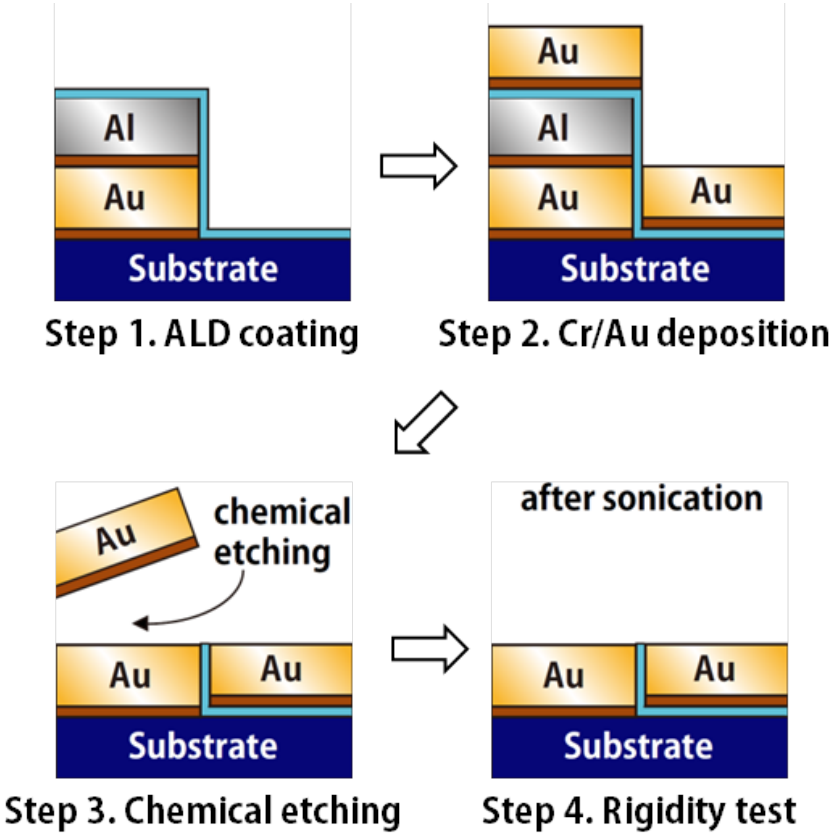

Figure 2.2: Role of a sacrificial layer in spacer-based nanogap fabrication processes.

an adhesive layer such as Cr or Ti in the second deposition of metals, and then to remove the excess layer by chemically etching a pre-defined sacrificial layer just above the first layer.

The procedure is depicted in Figure 2.2. In the first patterning step, a sacrificial layer is additionally deposited on top of the metal layer. Then, after atomic layer deposition of spacer material, the second metal layer is deposited with adhesive layer of Cr. Since wet etching of sacrificial layer

happens beneath the excess overhanging metal layer, removal of the excess layer can occur even with the use of adhesive layer in the second deposition process. This leads to a better adhesion for the second deposited metal layer and accordingly the whole sample. The nanogap can therefore form even under imperfect conditions such as non-vertical sidewalls of the first metal layer, greatly improving the fabrication throughput. The fabricated nanogap is also very robust to mechanical agitations, enabling repeated uses in various sensing applications.

Figure 2.3 shows scanning electron microscope (SEM) images of a rectangular ring nanogap array. Since photolithography is used to define the gap perimeter, uniform arrays over a large area can be realized. Also, conformal dielectric deposition with ALD guarantees uniform gap widths over the whole area. Throughout this work, all sub-30 nm nanogaps are fabricated with the above method, with aluminum oxide spacer within the gap unless otherwise specified to be etched out later.

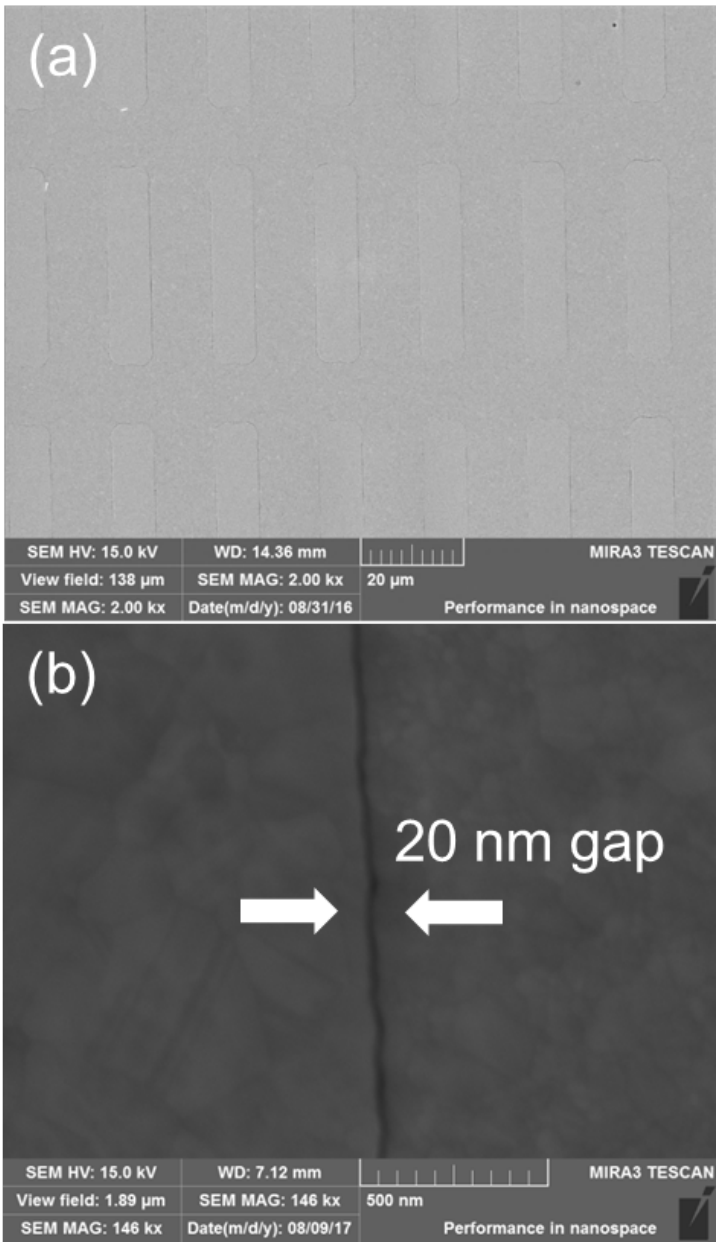

Figure 2.3: (a) Top-view scanning electron microscope image of a rectangular ring-shaped 20 nm gap array. (b) Magnified image of the 20 nm gap.

Chapter 3

Analytic solution for fields inside nanogaps

3.1 Modal expansion calculation

The most frequently used calculation tools in optics such as finite-difference time domain (FDTD) or finite element method (FEM) simulations are not very effective in calculating the terahertz nano-slots due to the huge mismatch of the structure size (orders of nanometers) to wavelength (hundreds of microns). Such limitations in computational capacity call for an analytic tool capable of predicting the performance of the terahertz nano slots. One of the first attempts was made by Garcia-Vidal et al., which is briefly introduced below[58].

First, under perfect electric conductor assumption for metal, we divide the slot antenna into three spaces: region above the metal (I), the gap (II), and region below the metal (III). Then we expand the electromagnetic field in the k-space with coefficients g and f for region I and III. Without loss of generality the terahertz wave is incident from region I, where the field distribution can be written as below.

$$H_y^I = \sqrt{\frac{\varepsilon_0}{\mu_0}} \int dk_x dk_y [\delta(k_x)\delta(k_y) e^{ik_{1z}z} + g_y(k_x, k_y) e^{i\Theta} e^{-ik_{1z}z}] \tag{3.1}$$

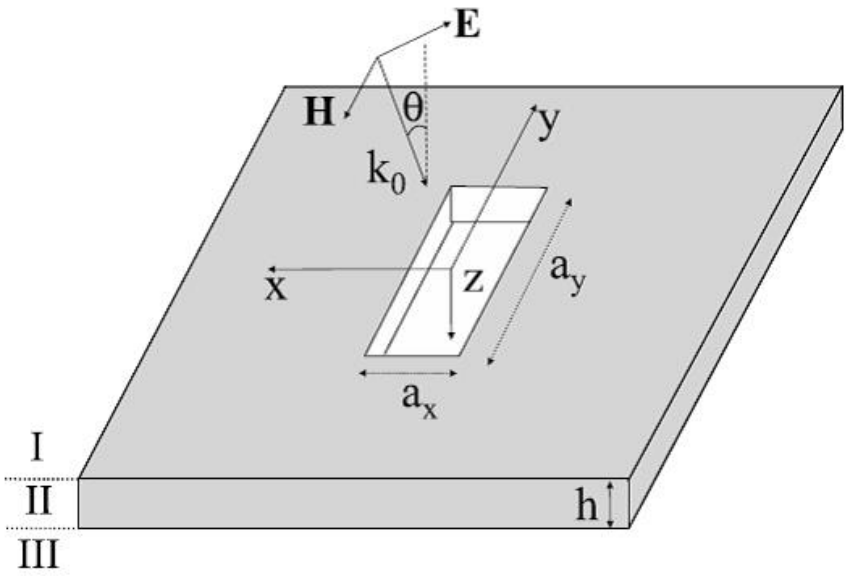

Figure 3.1: A slot antenna geometry used in the modal expansion calculation. Figure from Garcia-Vidal *et al*.

$$E_x^I = \frac{i}{k_0\varepsilon_1}\sqrt{\frac{\mu_0}{\varepsilon_0}}\left(\frac{\partial H_z}{\partial y} - \frac{\partial H_y}{\partial z}\right)$$
$$= \frac{i}{k_0\varepsilon_1}\int dk_x dk_y [g_z(ik_y)e^{i\Theta}e^{-ik_{1z}z} - \delta(k_x)\delta(k_y)(ik_{1z})e^{ik_{1z}z} + g_y(-ik_{1z})e^{i\Theta}e^{-ik_{1z}z}] \tag{3.2}$$

where $\Theta = k_x x + k_y y$. Here the first term in the expression for the magnetic field corresponds to incident wave, and the second term describes the reflected waves with dispersions given by mode coefficient. The integrations over k-space are replaced with summation with steps of $k_{x,y} = \dfrac{2\pi}{d_{x,y}}$ for array structures with periods $d_{x,y}$. Similarly fields in region III is expanded as:

$$H_y^{III} = \sqrt{\frac{\varepsilon_0}{\mu_0}}\int dk_x dk_y f_y(k_x,k_y)e^{i\Theta}e^{ik_{3z}(z-h)}] \tag{3.3}$$

$$E_x^{III} = \frac{i}{k_0\varepsilon_3}\sqrt{\frac{\mu_0}{\varepsilon_0}}(\frac{\partial H_z}{\partial y} - \frac{\partial H_y}{\partial z})$$
$$= \frac{i}{k_0\varepsilon_3}\int dk_x dk_y [f_z(ik_y)e^{i\Theta}e^{ik_{3z}(z-h)} - f_y(ik_{3z})e^{i\Theta}e^{ik_{3z}(z-h)}] \quad (3.4)$$

Finally, if the slot width is much smaller than the length we can assume that only one single mode dominates the gap region, and therefore the field in region II is written as:

$$E_x^{II} = \cos\frac{\pi y}{l}[Ae^{i\beta z} + Be^{-i\beta z}] \quad (3.5)$$
$$H_y^{II} = \frac{\beta}{k_0}\sqrt{\frac{\varepsilon_0}{\mu_0}}\cos\frac{\pi y}{l}[Ae^{i\beta z} - Be^{-i\beta z}] \quad (3.6)$$

Here $\beta = \sqrt{\varepsilon_2 k_0^2 - (\frac{\pi}{l})^2}$ is propagation constant of the rectangular waveguide mode. Boundary condition requires that electromagnetic fields in region I and II, II and III be continuous at the exit and entrance of the hole,

$$(1)H_y^I(z=0) = H_y^{II}(z=0) \quad (3.7)$$
$$(2)E_x^I(z=0) = E_x^{II}(z=0) \quad (3.8)$$
$$(3)H_y^{III}(z=h) = H_y^{II}(z=h) \quad (3.9)$$
$$(4)E_x^{III}(z=h) = E_x^{II}(z=h) \quad (3.10)$$

leading to following four equations,

$$\sqrt{\frac{\varepsilon_0}{\mu_0}}(1+\int dk_x dk_y g_y e^{i\Theta}) = \frac{\beta}{k_0}\sqrt{\frac{\varepsilon_0}{\mu_0}}\cos\frac{\pi y}{l}[A-B] \tag{3.11}$$

$$\frac{i}{k_0\varepsilon_1}[-i\sqrt{\varepsilon_1}k_0+\int dk_x dk_y i(g_z k_y + g_y k_{1z})e^{i\Theta}] = \cos\frac{\pi y}{l}[A+B] \tag{3.12}$$

$$\sqrt{\frac{\varepsilon_0}{\mu_0}}\int dk_x dk_y f_y e^{i\Theta} = \frac{\beta}{k_0}\sqrt{\frac{\varepsilon_0}{\mu_0}}\cos\frac{\pi y}{l}[Ae^{i\beta h}-Be^{-i\beta h}] \tag{3.13}$$

$$\frac{i}{k_0\varepsilon_3}\int dk_x dk_y i(f_z k_y - f_y k_{3z})e^{i\Theta} = \cos\frac{\pi y}{l}[Ae^{i\beta h}+Be^{-i\beta h}] \tag{3.14}$$

Then we express g_y and f_y explicitly as a function of $k_{x,y}$ by pulling them out of the integral via eigenmode projection,

$$g_y = \frac{k_x^2+k_{1z}^2}{k_0 k_{1z}}\frac{1}{(2\pi)^2}[\frac{(2\pi)^2}{\sqrt{\varepsilon_1}}\delta(k_x)\delta(k_y)-(A+B)\frac{wl}{2}J] \tag{3.15}$$

$$f_y = \frac{k_x^2+k_{3z}^2}{k_0 k_{3z}}\frac{1}{(2\pi)^2}[(Ae^{i\beta h}+Be^{-i\beta h})\frac{wl}{2}J] \tag{3.16}$$

where

$$J = \frac{2}{wl}\int_{hole} dxdy\cos\frac{\pi y}{l}e^{-i\Theta} \tag{3.17}$$

Putting the expressions for g and f back into the integral relation finally enables expressing field enhancement at the gap [A+B] or $[Ae^{i\beta h}+Be^{-i\beta h}]$ in terms of k,

$$\frac{8i}{\pi}-(A+B)G^I = i\frac{\beta}{k_0}(A-B) \tag{3.18}$$

$$(Ae^{i\beta z}+Be^{-i\beta z})G^{III} = i\frac{\beta}{k_0}(Ae^{i\beta z}-Be^{-i\beta z}) \tag{3.19}$$

where

$$G^{I,III} = \frac{i}{(2\pi)^2} \int dk_x dk_y \frac{k_x^2 + k_{1,3z}^2}{k_0 k_{1,3z}} \frac{wl}{2} |J|^2 \tag{3.20}$$

Here $G^{I,III}$ represents coupling of gap modes with region I and III, respectively, and J is a tranfer function through the rectangular gap. Solving for A and B leads to field profile inside the gap (region II), and subsequently fields in the whole area of interest. In terms of average electric field amplitude at the gap entrance $E = \frac{A+B}{\sqrt{2}}$ and the gap exit $E' = \frac{Ae^{i\beta z} + Be^{-i\beta z}}{\sqrt{2}}$, the solution looks like:

$$\begin{bmatrix} E \\ E' \end{bmatrix} = \frac{I_0}{(G^I - \Sigma)(G^{III} - \Sigma) - G_V^2} \begin{bmatrix} G^{III} - \Sigma \\ G_V \end{bmatrix} \tag{3.21}$$

where

$$\Sigma = \frac{\frac{\beta}{k_0}}{\tan \beta h}, G_V = \frac{\frac{\beta}{k_0}}{\sin \beta h}, I_0 = \frac{4\sqrt{2}}{\pi i} \tag{3.22}$$

The whole calculation therefore reduces to numerical calculation of $G^{I,III}$. The integrand quickly converges to 0 as $k_{x,y}$ becomes large, so the calculation load is relatively small. The resonance condition is when the propagation constant is zero, that is, $k_0 = \frac{1}{n_2}\frac{\pi}{l}$. The gap therefore can be treated as a simple waveguide where length of the cavity entrance and refractive index of the waveguide core has linear relationships with the resonant wavelengths.

The biggest assumption in this calculation is that there is no electromagnetic field smearing into the metal and the field is solely confined in the gap region. In terahertz frequencies, where refractive index of noble metal is

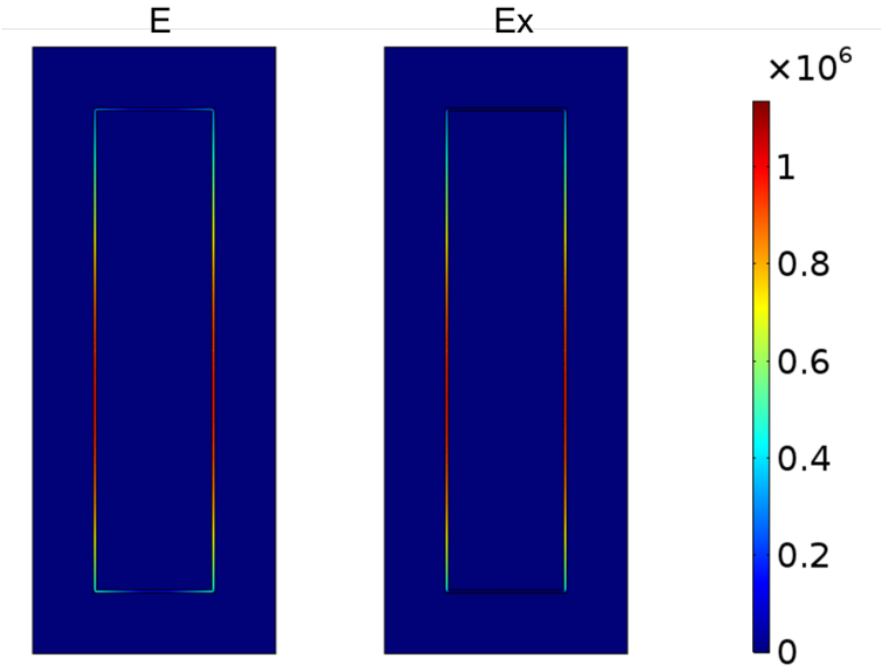

Figure 3.2: Electric field distribution of the lowest dipole mode in a rectangular ring waveguide. The field distribution is nearly sinusoidal along the ring contour, behaving effectively as a pair of identical rectangular slots.

1000+1000i, electromagnetic field inside the metal is smaller by a factor of 10^6, safely falling under the perfect electric conductor assumption in most cases.

One more issue worth pointing out is that fabrication of nanogaps with atomic layer lithography can only support nano-slots with ring geometry, while original paper by Garcia-Vidal et al. performed calculations on a rectangular hole. The field profile in region II therefore has to be appropriately modified to correctly represent the rectangular ring structure. Figure 3.2 shows a finite element method (FEM) simulation result for a coaxial rect-

angular waveguide structure. The lowest TE11 mode of a coaxial waveguide supports sinusoidal electric field distribution along its contour, such that electric field distribution in the short sides of the rectangular ring becomes antisymmetric. Therefore near fields from the long sides solely contribute to the observed far field transmission, and the rectangular ring can be effectively treated as a pair of truncated rectangular slots.

3.2 Modal expansion calculation with gap plasmon effect

When the gap is extremely small, a crosstalk between the two metal layers can occur and gap plasmon effect comes in to play. As beforementioned this leads to an increase in effective permittivity of the gap. Also, electric field from one side of the gap can significantly alter the field distribution of the other side of the gap. In this limit, which is gap width of 100 nm or below for terahertz frequencies, an additional wavevector smearing into metal layer from region II, denoted as k_x, must be considered[59]. For a symmetric structure with same metal used in each side of the gap, this is expressed as a cosh-type distribution of the electric field (which was previously constant in the x direction). The calculation scheme is briefly depicted in Figure 3.3. To begin with, now that electromagnetic field of all polarizations are present in the gap (in contrast to perfect electric conductor case, where only Ex, Hy and Hz are present for the fundamental TE mode of the waveguide), now Hy is determined by both Ex and Ez. The electromagnetic

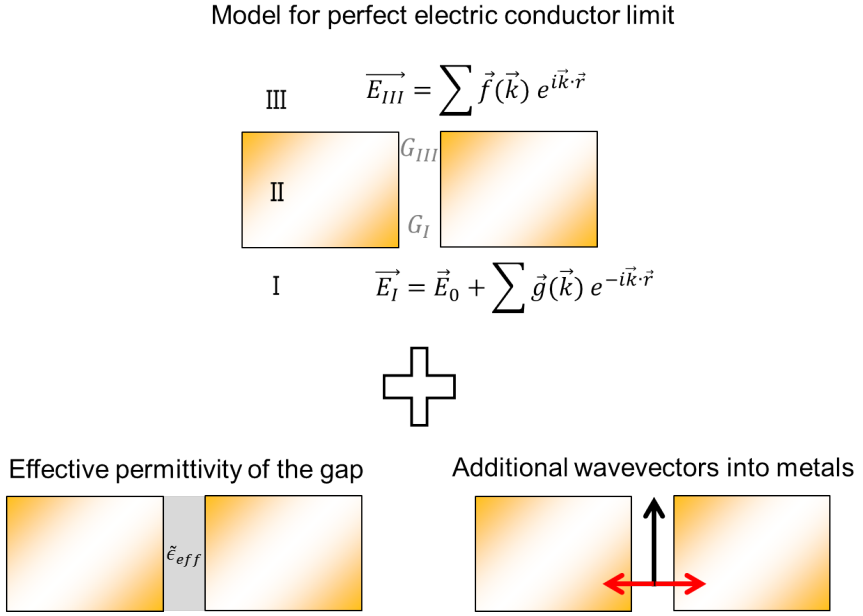

Figure 3.3: Schematics of modal expansion calculation with gap plasmon effect added. Changes in effective permittivity of the gap and changes in electric-to-magnetic field ratio induced by the additional smearing wavevector must be taken into account.

field distribution inside the gap is therefore given as:

$$E_x^{II} = \cosh(k_x x)\cos(\frac{\pi y}{l})[Ae^{i\beta z} + Be^{-i\beta z}] \tag{3.23}$$

$$H_y^{II} = \frac{\beta}{k_0}\frac{1}{1+\frac{k_x^2}{\varepsilon_2 k_0^2}}\sqrt{\frac{\varepsilon_0}{\mu_0}}\cos\frac{\pi y}{l}[Ae^{i\beta z} - Be^{-i\beta z}] \tag{3.24}$$

Here, k_x is the gap plasmon wavevector k_2 from section 1.3. Also, the propagation constant should be altered in order to satisfy momentum conservation:

$$\beta = \sqrt{\varepsilon_2 k_0^2 - (\frac{\pi}{l})^2 + k_x^2} \tag{3.25}$$

Following the procedure in Chapter 3.1 leads to a set of equations,

$$\frac{8i}{\pi} - (A+B)G^I = i\frac{\beta}{k_{0,eff}}(A-B) \tag{3.26}$$

$$(Ae^{i\beta z} + Be^{-i\beta z})G^{III} = i\frac{\beta}{k_{0,eff}}(Ae^{i\beta z} - Be^{-i\beta z}) \tag{3.27}$$

where

$$k_{0,eff} = k_0 \times (1 + \frac{k_x^2}{\varepsilon_2 k_0^2}) \tag{3.28}$$

Note that this equation returns to the perfect electric conductor case when $k_x = 0$. The increase in propagation constant means that light travels slower inside the gap; that is, existence of the gap plasmon leads to a red-shift in the spectrum of the nanogap. Also, since k_x is a complex number, an imaginary part is introduced to the effective refractive index of the gap. Under strong influence of the gap plasmon, therefore, a decrease in gap width is expected to result in smaller and red-shifted transmission.

Figure 3.4 shows the effect of gap plasmon on calculated transmission spectrum of terahertz nanogaps. To observe the gap plasmon effect exclusively, the whole structure is assumed to be free-standing without a supporting dielectric. Compared to transmission spectra of nanogaps under perfect electric conductor assumption, those of real metal calculation show much broader and red-shifted resonance. The differences in the spectra are not so distinct in gaps broader than 100 nm, yet becomes much bigger as the gap width reduces.

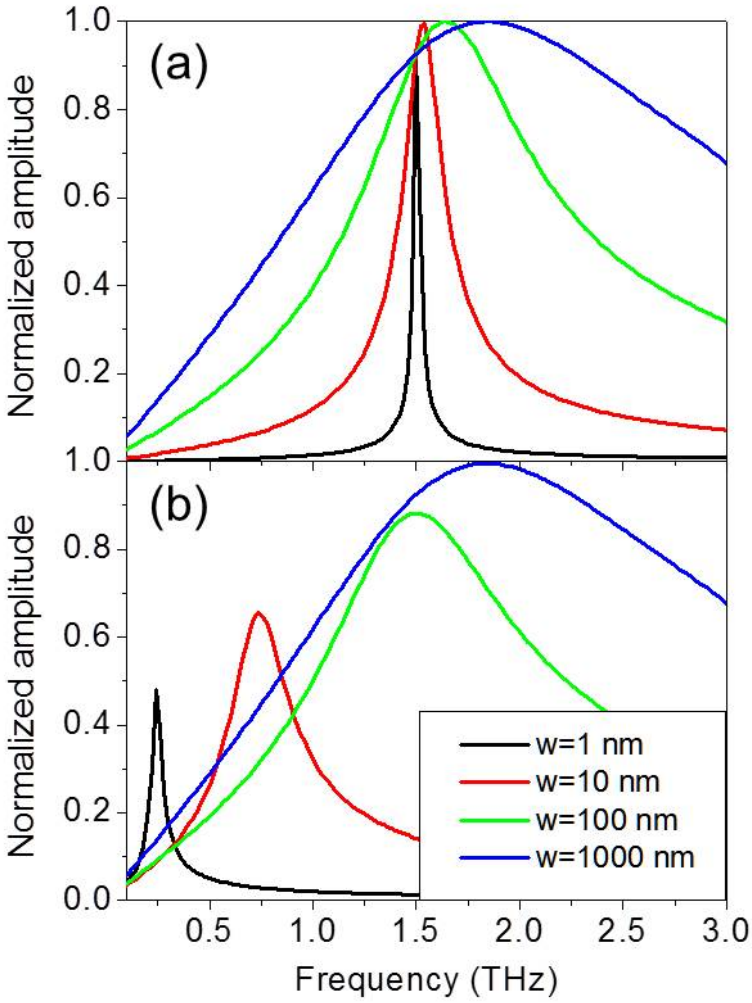

Figure 3.4: Calculated transmission spectra of slot antennas with different widths. (a) PEC-assumed spectra, showing relatively small resonance shift and transmission level. (b) Real metal calculation, showing a strong influence of gap plasmon modes in gap widths smaller than 100 nm.

Chapter 4

Index-matching effect of substrate on nanogaps

4.1 Index-matching of a substrate on a thin metal film

Dielectric substrates usually have high refractive index at THz frequencies ($n_{Si} = 3.41, n_{sapphire} = 3.2$, etc.). Such properties are useful in index matching, where existence of a dielectric increases coupling of light with a target system[60]. While such effects are predominantly utilized in photovoltaic applications in visible wavelengths[61, 62], such index-matching effects are also realized in THz frequencies.

For instance, Figure 5.1 shows a set of calculations where existence of a silicon substrate ($n_{Si} = 3.4$) significantly alters the absorption behavior of a thin Au film. A simple Fresnel coefficient analysis with multiple reflection effects leads to following expressions for transmission, reflection and

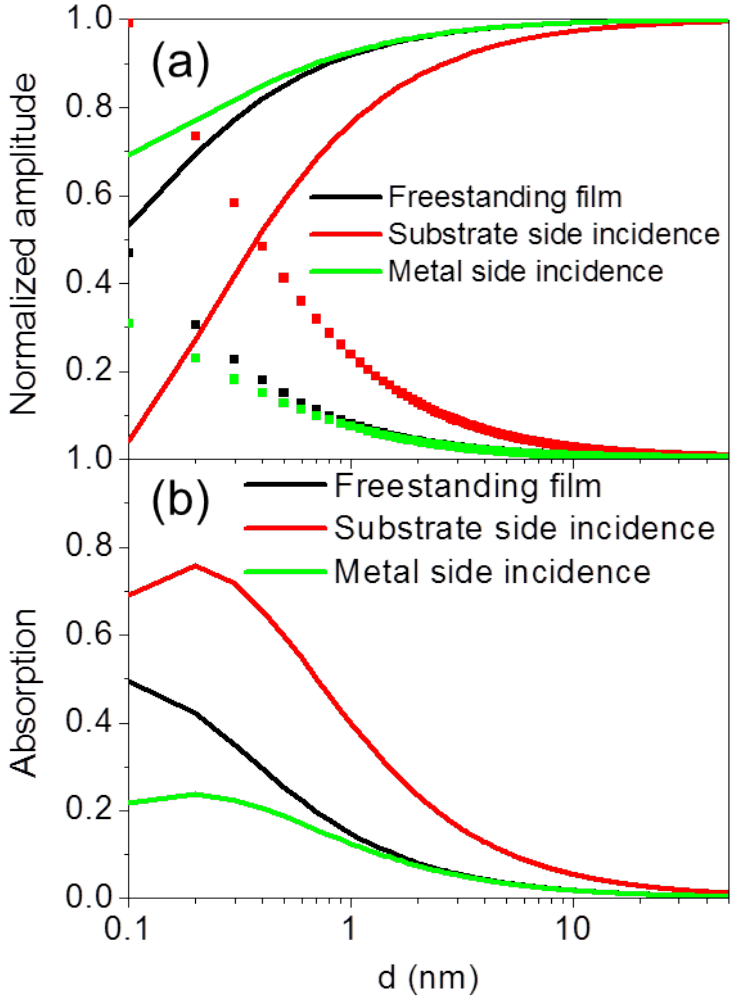

Figure 4.1: (a) Transmitted (dots) and reflected (lines) amplitudes from freestanding and silicon substrate-backed Au thin films. The transmission and reflection change upon changing the incident side. (b) Absorption of terahertz waves by thin gold films that are freestanding or supported by a silicon substrate. Substrate side incidence show higher absorption due to index matching effect by the substrate.

absorption[63],

$$t = \frac{t_{12}t_{23}e^{2i\beta}}{1 + r_{12}r_{23}e^{2i\beta}} \tag{4.1}$$

$$r = \frac{r_{12} + r_{23}e^{i\beta}}{1 + r_{12}r_{23}e^{2i\beta}} \tag{4.2}$$

$$A = 1 - r^2 - \frac{n_3}{n_1}t^2 \simeq \frac{\frac{4n_1\varepsilon_0 c}{\sigma h}}{(1 + \frac{(n_1 + n_3)\varepsilon_0 c}{\sigma h})^2} \tag{4.3}$$

where subscripts 1, 2, and 3 denotes incident area, metal film and transmitted area, respectively, and h is thickness of the film, and σ is DC conductance of the Au film. The last approximation works for small direct transmission and sub-wavelength thickness of the Au film. While noble metals are nearly perfectly conducting and highly reflective in millimeter wavelengths, the very thin film of gold can absorb up to 50 percent of incident THz power if the film is 1 Angstrom thick. This is possible due to multiple reflections within the film and correspondingly large electric field induced inside the metal. In presence of a substrate, however, the film transmits and absorbs terahertz waves better due to the index matching effect. With substrate index of 3.41, the maximum absorption reaches 75 percent at 2 Angstrom thickness. The effect is reversed when the THz wave is incident from the opposite side. The side of incidence is therefore a crucial factor in coupling of an absorbing film with the incident electromagnetic waves, especially when the substrate supporting the film has a large refractive index.

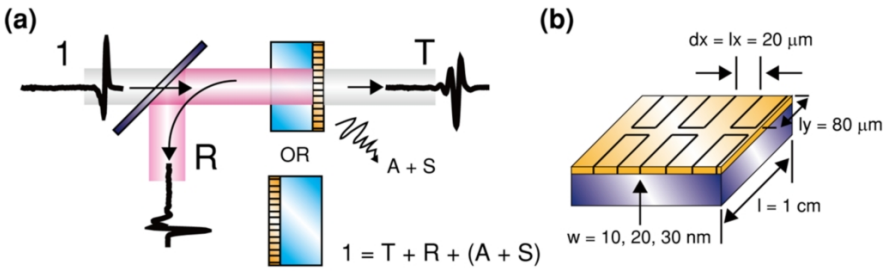

Figure 4.2: (a) Schematic of the transmission and reflection experiments. (b) Nanogap sample dimensions.

4.2 Transmission

The effect of substrate on optical properties of nanogaps are investigated. THz transmission and reflection of nanogaps with widths 10, 20 and 30 nm are measured with a home-made terahertz time-domain spectroscopy setup. The nanogaps are rectangular ring-shaped, due to fabrication requirements of the atomic layer lithography method, with 20 um and 80 um lengths for each sides of the rectangle. The nanogaps are fabricated on top of silicon substrates (n = 3.41), and are measured in either substrate side- or metal side-incidence to observe the effect of index matching by the substrate. A bare silicon substrate and 200 nm-thick Au film on a silicon substrate are used as references for transmission and reflection measurements, respectively. The experimental scheme is briefly described in Figure 4.2.

Figure 4.3 shows the incident side dependence of nanogap transmission. The normalized transmission for substrate side- and metal-side illuminations are the same, as expected for ordinary multilayer system. Yet local field distribution can be different, since electric field increases when exiting

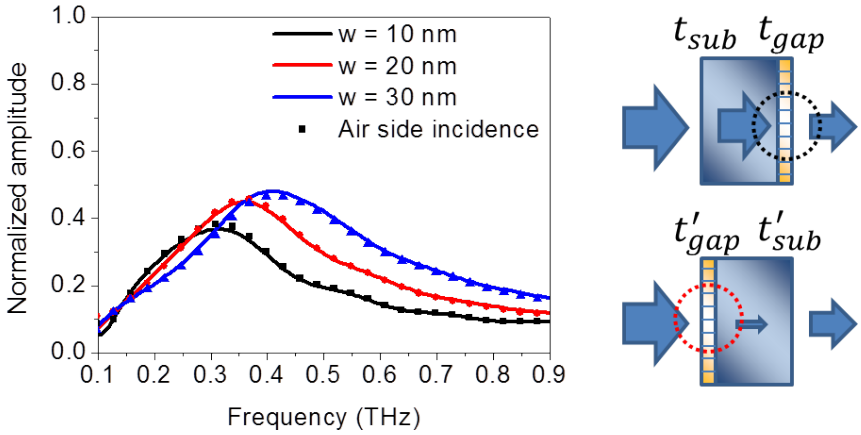

Figure 4.3: Transmitted amplitude through the nanogaps. Same transmission despite different Fresnel coefficients in the two cases imply different near field enhancements.

a dielectric while it decreases when entering it. A simple Fresnel coefficient analysis gives transmitted amplitude from air to a dielectric with refractive index n as

$$t_{sub} = \frac{2}{n+1} < 1 \tag{4.4}$$

and that from a dielectric to air as

$$t'_{sub} = \frac{2n}{n+1} > 1 \tag{4.5}$$

Since overall transmission is the same,

$$t = t_{sub} t_{gap} = t'_{gap} t'_{sub} \tag{4.6}$$

where t_{gap} and t'_{gap} denotes transmitted amplitude through nanogaps in sub-

strate side and metal side incidence, respectively. From Kirchhoff integral formalism introduced in Chapter 1.3, near field enhancement factor for each case is given as

$$FE = \frac{t}{\beta} FE' = \frac{\frac{t}{t'_{sub}}}{\beta} \tag{4.7}$$

which leads to following relation on near field enhancements under different illumination sides,

$$FE = FE' \times \frac{2n}{n+1} \tag{4.8}$$

Therefore the near field enhancement is larger for the substrate-side incident case by a factor of $\frac{2n}{n+1}$, even with smaller incident electric field amplitude in front of the gap. If the nanogaps array can be considered as an effective medium, the substrate can be said to have functioned as an index matching layer, enhancing the coupling between incident radiation and the medium. It is also worth noting that the factor $\frac{2n}{n+1}$ is the same as the ratio of incident magnetic field amplitude at the gap, as depicted in Figure 4.4. This implies the role of magnetic field and surface current on the field enhancement of nanogaps[64, 65], whereas electric field and surface charge can in principle perform the same role in a more simple structure.

As a means to directly confirm the near field enhancement, a power dependent transmission measurement is performed on the nanogaps fabricated on top of silicon substrates. It is known that V/nm orders of THz electric field in metal-dielectric-metal gap can induce transient tunneling current, causing higher absorption of THz waves inside the gap[66, 67]. Resulting decrease in THz transmission can therefore function as a direct probe of

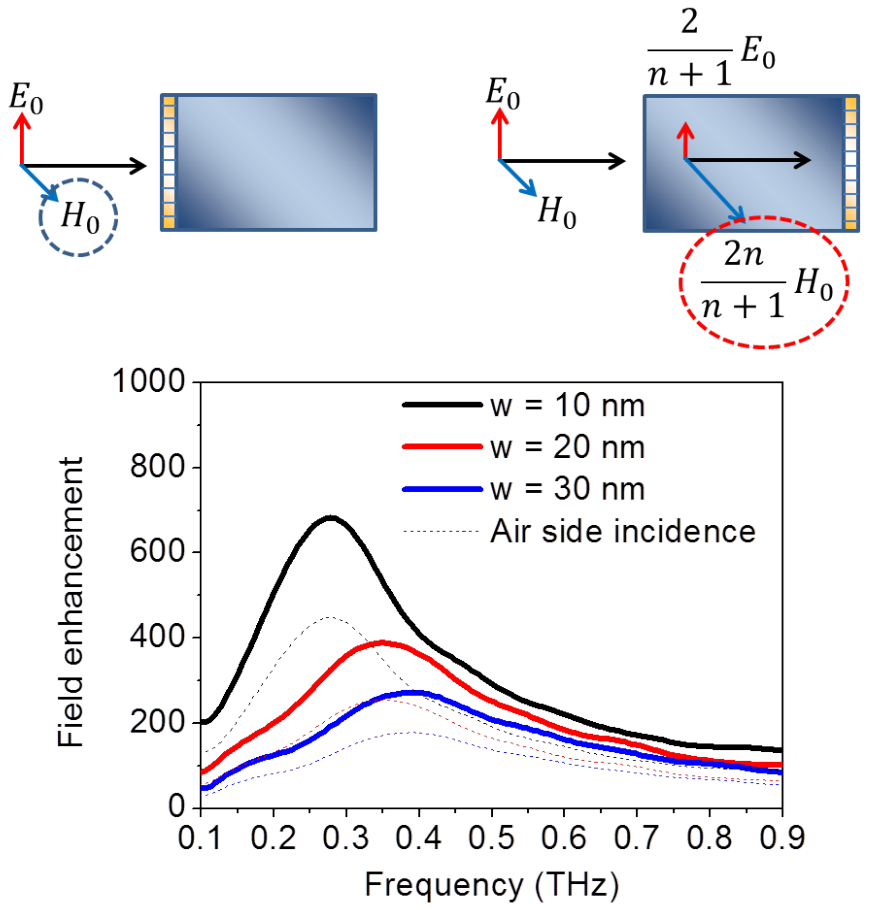

Figure 4.4: Role of magnetic field in the near field enhancement at nanogaps.

near field enhancement inside the gap.

Here, intense THz pulses with peak amplitude of 460 kV/cm are generated via tilted-pulse rectification from a lithium niobate crystal, and the amplitude is adjusted with a pair of wire grid polarizers. With the aid of field enhancement inside the gap by a factor of several hundreds, an instantaneous field amplitude exceeding V/nm is realized inside the gap. Figure 4.5

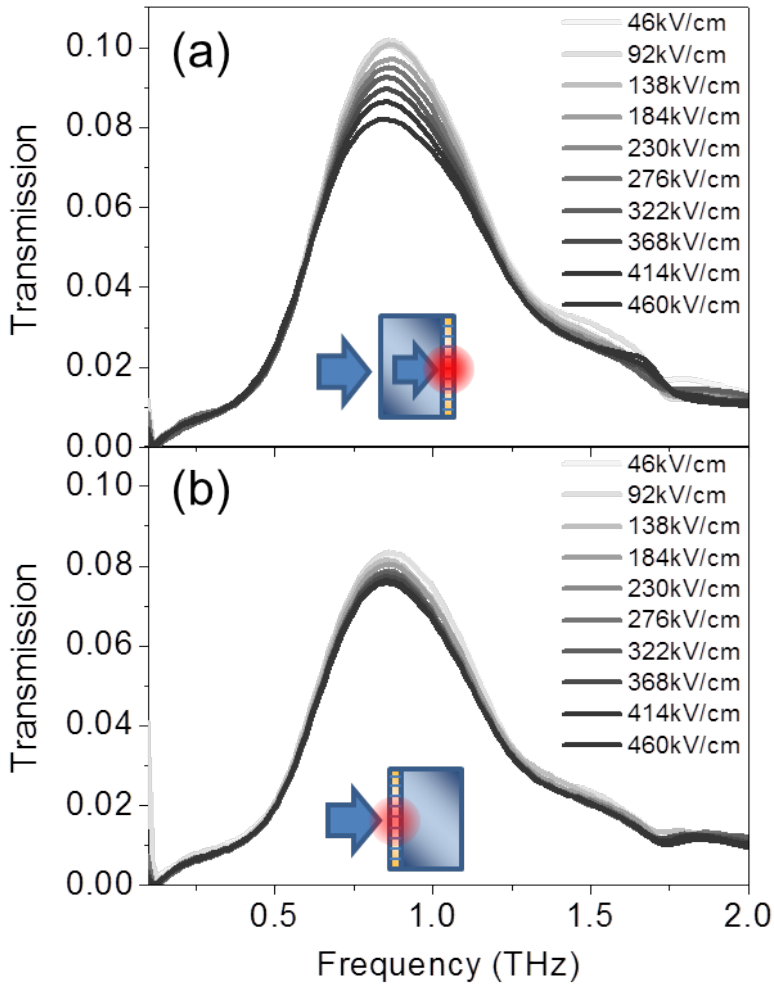

Figure 4.5: Power dependent transmission of a nanogap under (a) substrate side incidence, and (b) metal side incidence. Substrate side incidence induces larger decreases in transmission, that is, larger field enhancement.

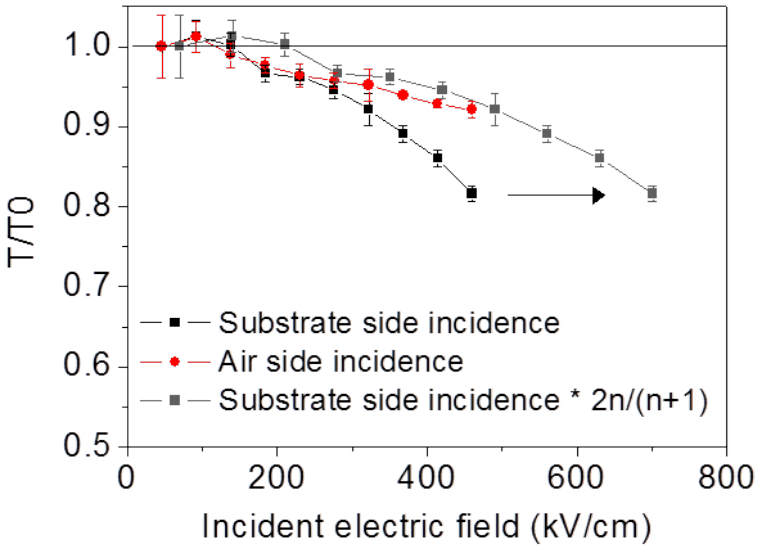

Figure 4.6: Power dependent transmissions of a nanogap under different incident sides, aligning to a single curve under implementation of a factor $2n/(n+1)$, where n is refractive index of the silicon substrate.

shows the result. Nanogaps show decreased transmission upon irradiation of the intense terahertz radiation, both in metal- or substrate-side incidence. Yet the power dependent transmission shows steeper decrease in transmission for the substrate-side incidence. This means that electric field inside the gap is larger in the gaps with substrate-side incidence. Moreover, when we plot the incident field-dependent relative transmissions for the both cases, the two curves align to a single one when the factor $\frac{2n}{n+1}$ considered in the electric field of the substrate-side incidence (Figure 4.6).

To further confirm that the index matching effect solely comes from the substrate, the same experiment is performed on a nanogap fabricated on a quartz substrate ($n = 1.2$). The gap material is also changed from ALD-

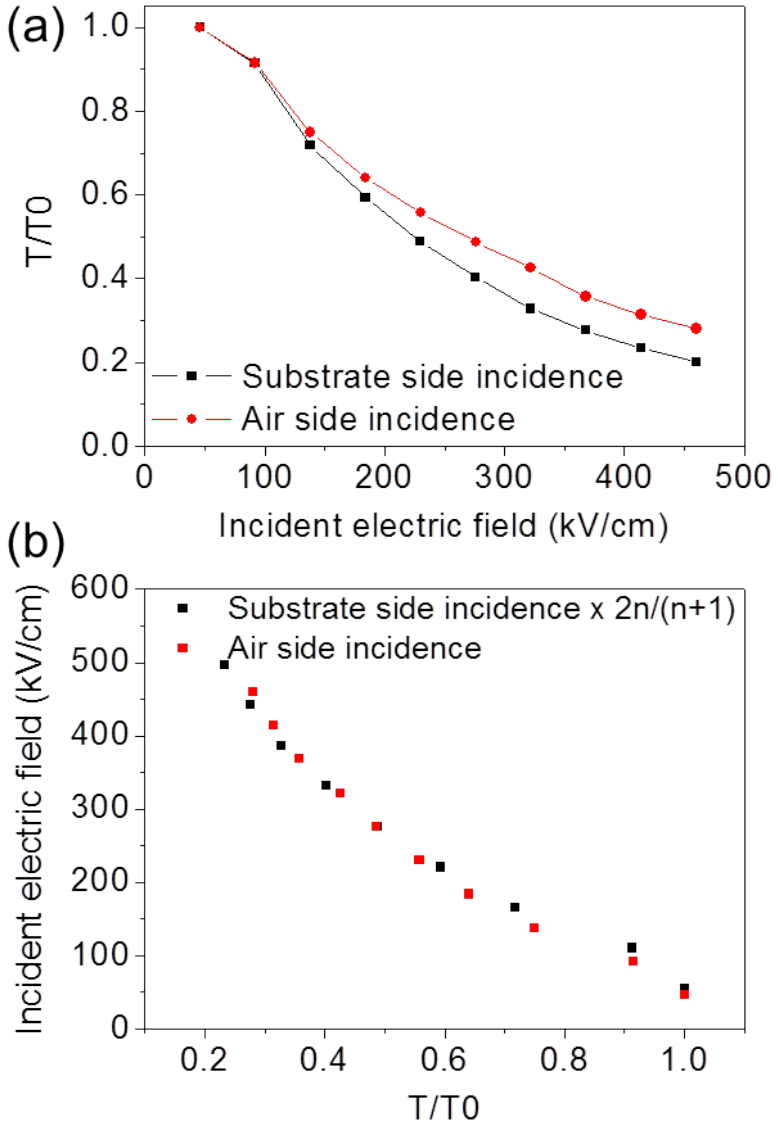

Figure 4.7: Power dependent transmission of a graphene gap, fabricated on top of a quartz substrate instead ($n = 1.2$). (a) Incident field dependent transmission curve. (b) Two curves aligning to a single one by multiplying the factor $\frac{2n}{n+1}$. The totally different gap also follows the factor, confirming the role of index matching by the substrate.

deposited aluminum oxide to multilayer graphene. The graphene gap is fabricated by growing graphene on a patterned copper film via chemical vapor deposition (CVD), followed by second deposition of copper and subsequent exfoliation step [66]. The result is presented in Figure 4.7. Even with completely different types of gap material, metal and substrate, the incident side dependent curves follow the same rule governed by the factor $\frac{2n}{n+1}$. This directly confirms the role of index matching of a substrate on the field enhancement inside the gap.

4.3 Reflection

While most studies on the slot structure utilizes transmitted amplitudes through the gap, few reports on reflection exists. Yet reflection is essential in quantifying absorption from the gap, and is also beneficial in selectively sensing the surface of a target system on top of the gap without accessing its bulk properties. Reflection from the nano-slots can be considered to consist of two components: (1) direct reflection from the metal part, and (2) scattering of the enhanced field at the gap. Depending on the relative phase, the two will either constructively or destructively interfere. At resonance of a nanogap, electric field at the gap is expected to be in phase with the incident THz wave. Since the reflected wave from metal is out of phase with the incident field, the two components will destructively interfere at resonance to result in a reflection dip, as depicted in Figure 4.8. While off-resonant component of the electric field is mostly imaginary, that is, phase-shifted by 90 degrees, resonant component is real, or on-phase with the incident field.

The total reflected power will be given as $S_z^I = -\frac{1}{2}E_x^I H_y^{I*}$. From Chapter 3, electromagnetic field in the whole region can be expanded in terms of field enhancement at the gap [A+B]. Ignoring the incident wave, the electromagnetic field in the reflection side is given as:

$$E_x^I = -\frac{1}{\sqrt{\varepsilon_I}}e^{-ik_{1z}} + \sum_{k_x,k_y}\frac{wl}{d_x d_y}[A+B]e^{i\Theta}e^{-ik_{1z}} \tag{4.9}$$

$$H_y^I = \frac{\varepsilon_0}{\mu_0}(e^{-ik_{1z}} - \sum_{k_x,k_y}\frac{wl}{d_x d_y}\frac{k_{1z}^2+k_x^2}{k_0 k_{1z}}[A+B]e^{i\Theta}e^{-ik_{1z}}) \tag{4.10}$$

When the nanogap array is sub-wavelength, which is indeed the case for the sample we use ($20\mu m, 80\mu m < 300\mu m$), only components with $k_{x,y} = 0$ contribute to the far field radiation. We obtain reflectance by normalizing the reflected power with respect to reflection from bare film,

$$R = 1 - \frac{4n_1 wl}{\pi dxdy}Re(E_{gap}) + \frac{4\varepsilon_1 w^2 l^2}{\pi^2 dx^2 dy^2}|E_{gap}|^2 \tag{4.11}$$

Figure 4.9 shows measurements and calculations for the 10, 20 and 30 nm gaps used in the transmission experiments. The reflection dip is larger for samples with higher resonance transmission, as expected from the interfering nature. Also the reflection dip is larger when THz radiation is incident from the substrate side. This can be interpreted as a consequence of higher field enhancement at the gap aided by the index matching effect.

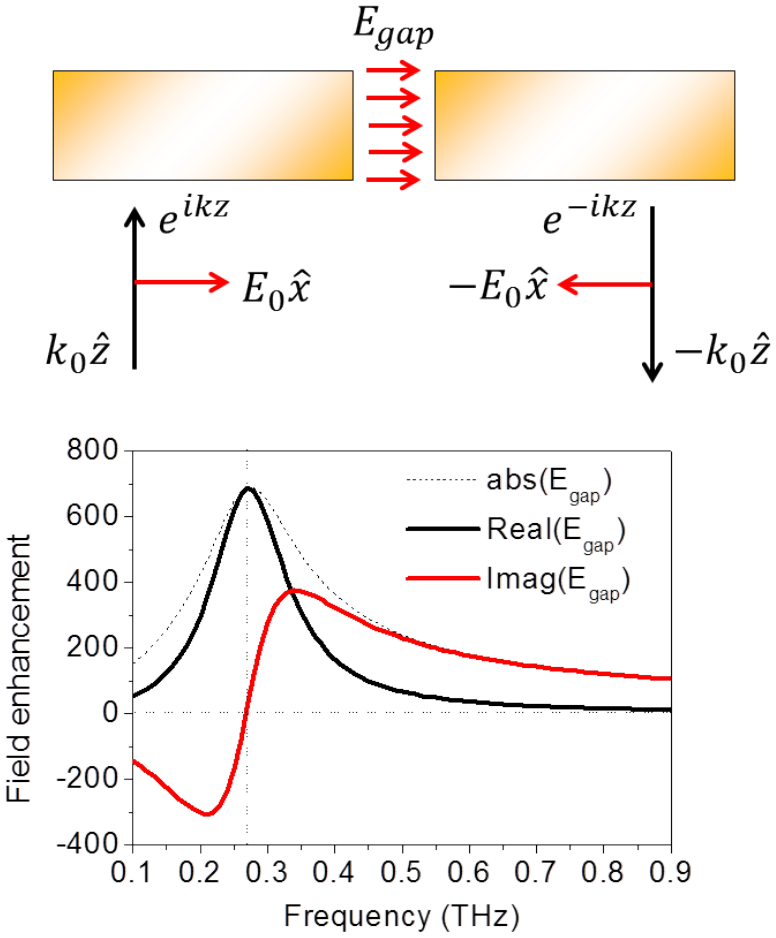

Figure 4.8: (a) Phase relation between the enhanced field at the gap and reflected field from the metal. (b) Calculated real and imaginary part of E_{gap} in a 10 nm gap. At resonance the E_{gap} is in phase with the incident wave, while at off resonance there exists a $\pi/2$ phase difference.

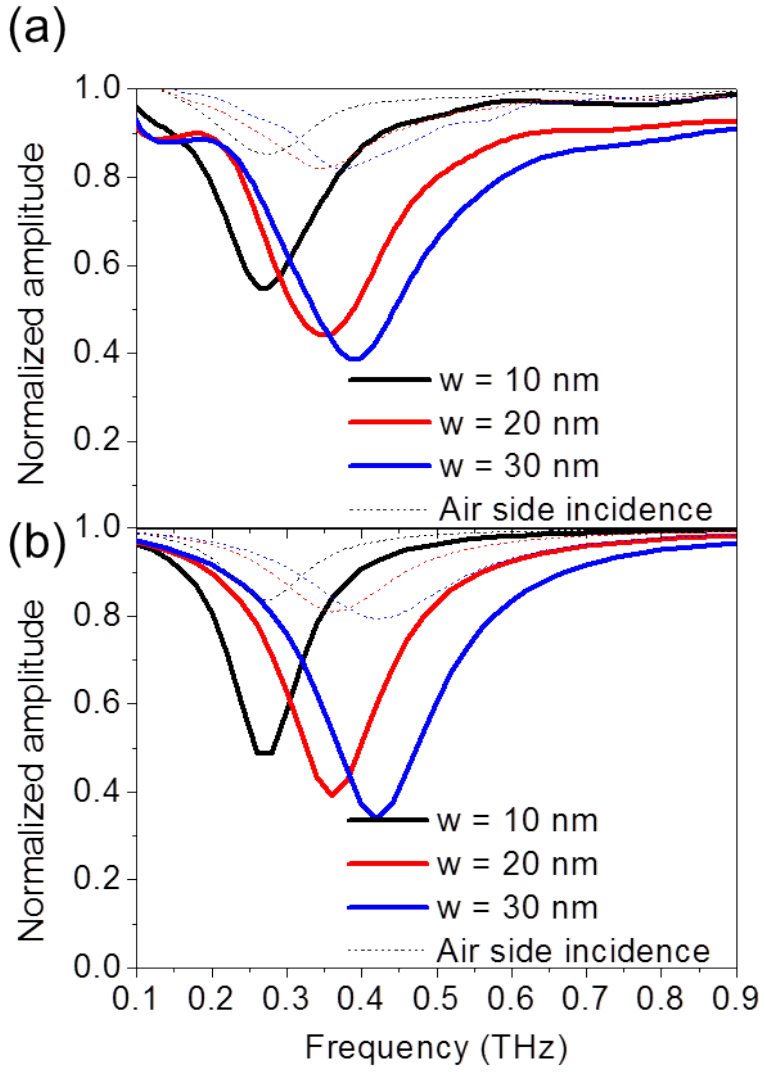

Figure 4.9: (a) Experimentally and (b) theoretically obtained reflection spectra of 10, 20 and 30 nm gap arrays.

4.4 Anomalous Ohmic absorption of THz waves in nanogaps

With metal surface sufficiently smooth and the nanogaps being extremely sub-wavelength in both gap sizes and periods, there's no scattering or surface waves, and the observed extinction can therefore be directly interpreted as absorption[68]. From the above results on transmission and reflection, the absorption from the nanogaps can directly be calculated via $T+R+A=1$.

Figure 4.10 shows the experimentally and theoretically determined absorption from the gap. Both experiments and calculations show absorption of above 60 percent. The absorption is Ohmic, since both gap material (alumina) and silicon substrates are nearly lossless. Yet Ohmic loss is proportional to $J \times E = \sigma E^2$, where J is current density, implying that electric field inside metal is very large despite the extremely large electric permittivity of the metal.

To figure out the origin of the huge Ohmic absorption we analyze the electric fields, or equivalently currents flowing in the metal near the gap ($J = \sigma E$). Figure 4.11 depicts the electromagnetic fields and current densities around a slot antenna. In a resonant slot antenna, two electric field components - E_x^M and E_y^M - are responsible for the field enhancement observed, where superscript M denotes field inside the metal. E_x^M drives capacitive current via direct transmission through metal film, and E_y^M creates inductive current around the slot which is responsible for resonant charge distribution.

We first examine E_x^M, which exists both far away from and near the

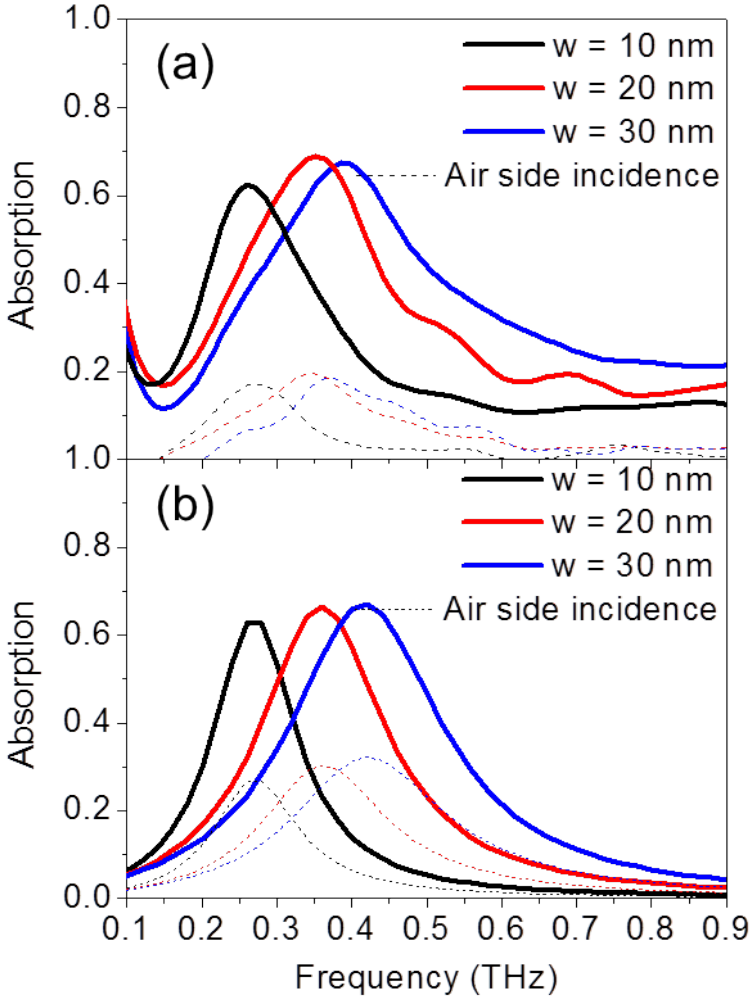

Figure 4.10: Terahertz absorption from nanogaps. Both (a) experiment and (b) theory expect absorption of over 60% in the sub-30 nm nanogaps.

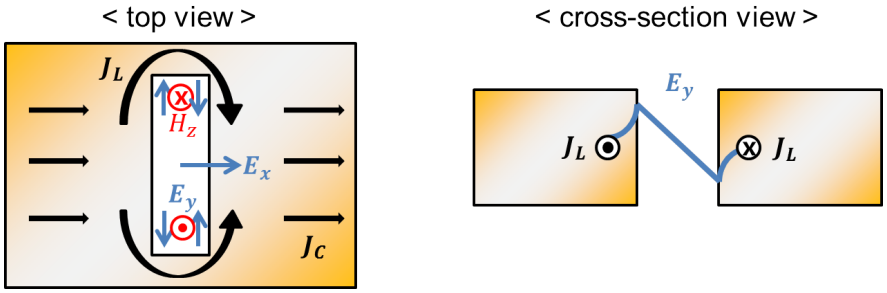

Figure 4.11: Field and current distribution around a resonant slot.

gap. The electric field far away from the gap would be nearly the same as that of direct transmission through bare film of same thickness, which is order of 5×10^{-4} times smaller than the incident electric field. At vicinity of the gap, the E_x^M is now determined from Maxwell continuity equation $D_{1,n} = D_{2,n}$, where 1 and 2 denotes inside the gap or metal. For a gap with field enhancement of 1000, electric permittivity contrast of 10^6 allows only 10^{-3} of incident field to smear into the metal. Absorption induced by capacitive current is therefore very small ($\sim 10^{-4}$) and the anomalous absorption observed therefore must come from the inductive current.

The inductive current is driven by Hz or equivalently Ey, which is expressed in the analytic calculation as:

$$H_z = \frac{k_y}{k_{0,eff} Z_0} \cosh(k_1 x) \sin(k_y y) [A e^{i\beta h} + B e^{-i\beta h}] \tag{4.12}$$

$$E_y = \frac{1}{-i\omega\varepsilon_0\varepsilon_d} \frac{\partial H_z}{\partial x} \tag{4.13}$$

$$= \frac{k_y k_1}{\varepsilon_d k_{0,eff} k_0} \sinh(k_1 x) \sin(k_y y) [A e^{i\beta h} + B e^{-i\beta h}] \tag{4.14}$$

where $k_{0,eff} = k_0 \times (1 + \frac{k_1^2}{\varepsilon_d k_0^2})$. Note that E_y increases as k_1 increases, that is, as gap plasmon effect becomes stronger. Continuity of parallel electric field in the metal-gap interface leads to an expression of the electric field inside the metal,

$$E_y^M = E_y(x = \frac{w}{2}) \times e^{-k_3(x - \frac{w}{2})} \tag{4.15}$$

This electric field is therefore localized within a distance of skin depth fom the slot. This electric field drives the inductive current $J_L = \sigma E_y$, which in turn leads to rate of dissipation of energy per unit volume in ohmic loss, $J_L E_y$. Since Ey can only be induced in a resonant structure, the absorption is only possible in slots; infinite slits, for example, lack the inductive current and therefore only minute absorption from capacitive current is expected to occur. Time average and volume integral of $J_L E_y$ leads to normalized absorption with respect to incident power,

$$Abs_{norm} = (\frac{k_1^2}{k_0^2 + k_1^2} \frac{k_y w}{2} \times E_{gap})^2 \times \frac{l}{2} \times \frac{\sigma h}{2Im(\sqrt{\varepsilon_M})k_0} / \frac{P_0}{Area} \tag{4.16}$$

Figure 4.12 shows the calculation results for absorption at resonance and corresponding electric field amplitude at various widths. Calculations show that smaller width leads to stronger E_y^M inside metal, and the amplitude reaches near 30 percent of that of incident field. This is more than 2 orders of magnitude larger than E_x^M near the gap. Together with high electric conductivity of gold ($\sigma_{Au} = 4 \times 10^7 S$), this giant electric field result in Ohmic absorption of over 70 percent in theory. This is by far the largest Ohmic absorption reported in metamaterial absorbers operating in

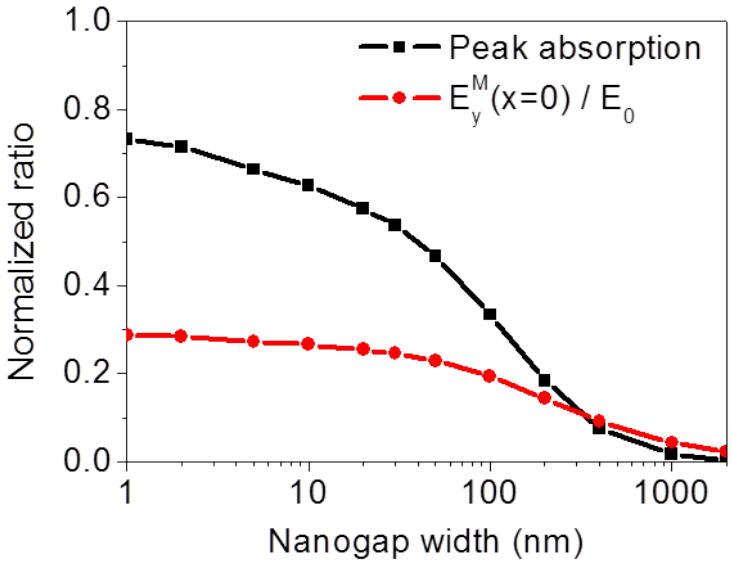

Figure 4.12: Ohmic absorption by a resonant slot. As the gap width decreases, inductive component of electric field near the slot reaches near 30% of incident field and peak absorption exceeds 70% in a 1 nm gap.

THz frequencies[69, 70]. This is also equivalent to THz absorption by gold film of 2 Angstrom thickness on top of a silicon substrate, which is a 1000-fold decrease of effective thickness from the original thickness of 200 nm.

It is worth noting that the absorption spectrum calculated from the field-current analysis completely matches that from transmitted and reflected spectrum, as shown in Figure 4.13, even with the totally different calculation procedure. Here possible effects from surface resistivity of Au film is neglected, which might be a cause of overestimation of field enhancement. Nevertheless the most dominant mechanism for the observed absorption is the inductive current, revealing a novel path for realization of terahertz metamaterial absorbers.

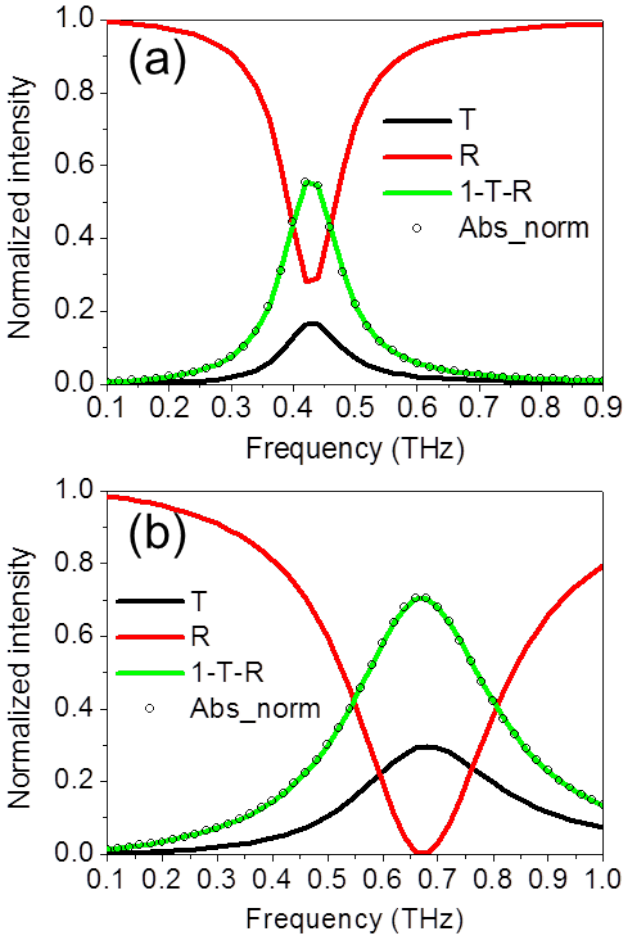

Figure 4.13: Calculated absorption from field-current analysis (Abs_{norm}) and from transmission and reflection spectra (1-T-R) on two different structures, (a) w=2 nm, n_1 = 1.4 and (b) w=10 nm, n_1 = 3.4. For both of the structures, the two calculations predict the same absorption spectra.

Chapter 5

Coupling terahertz nanogaps with liquid water

5.1 Optical properties of liquid water at THz frequencies

Water is a very interesting system to investigate as much as it is important to many chemical and biological phenomena. For example, water molecules show eccentric behaviors at interfaces of biological molecules[71, 72, 73, 74], metallic surfaces[75, 76], dielectrics[77], graphene[78, 79], etc.. In terms of applications, water desalination[80, 81] and electrolysis[82, 83] have been extensively investigated for decades.

In terahertz frequencies, water molecules in liquid phase show strong intermolecular interaction due to hydrogen bond network, exhibiting a broad resonance corresponding to a rotational relaxation mode at 5 THz[84, 85, 86]. Low THz frequencies (0.1$\sim$1 THz) correspond to a low-frequency tail of the mode, and here liquid water shows relatively high absorption coefficient. The complex refractive index of liquid water is 2.1 + 0.6i at 1 THz, which corresponds to an absorption coefficient of $250cm^{-1}$ (Figure 5.1). This is several times larger than values of other well-known terahertz absorbing molecules such as lactose or RDX[43].

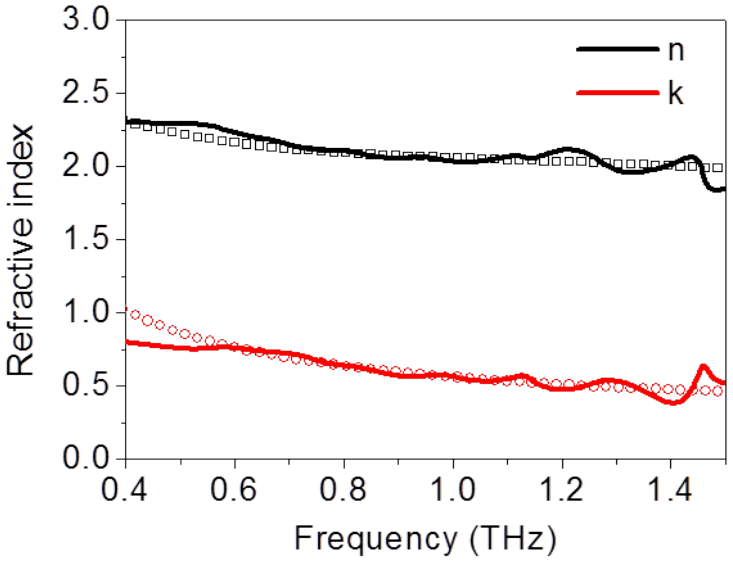

Figure 5.1: Real and imaginary parts of refractive index of water retrieved from transmission through 250 micron thick water layer. Dots refer to reported values from literatures.

5.2 Accessing the hot spots of spacer-based nanogaps

As briefly introduced in section II.1, the spacer-based fabrication is by far the only way to reliably access sub-10 nm gaps with arbitrary shapes and sizes. Yet the spacer-based nanogaps are incapable of coupling other materials into their hot spots due to presence of the spacer, showing limited applicability. It would therefore be beneficial to realize an empty, sub-10 nm gap by etching out the spacer.

We performed wet etching of nanogaps with alumina spacer within their gaps, with 1M potassium hydroxide (KOH) as the wet etchant. After etching, cross-sectional transmission electron microscope (TEM) images are taken to confirm the full etching of the alumina spacer. Figure 5.2 shows the results, where an energy dispersive spectroscopy is performed on a TEM cross sectional samples of an alumina-filled gap and an etched out gap. The disappearance of Al peak inside the gap after the etching confirms the full etching of the spacer. The structure also retains its shape after etching, confirming that proper etching procedure can prevent the nanogap structure from collapsing.

While it seems unlikely that water and etchant molecules enter such narrow and deep gaps in a short period of time, it can be explained in terms of wettability of a surface. The wettability of a surface can be quantified in terms of a spreading parameter S,

$$S = \gamma_{S-A} - \gamma_{L-A} - \gamma_{S-L} \tag{5.1}$$

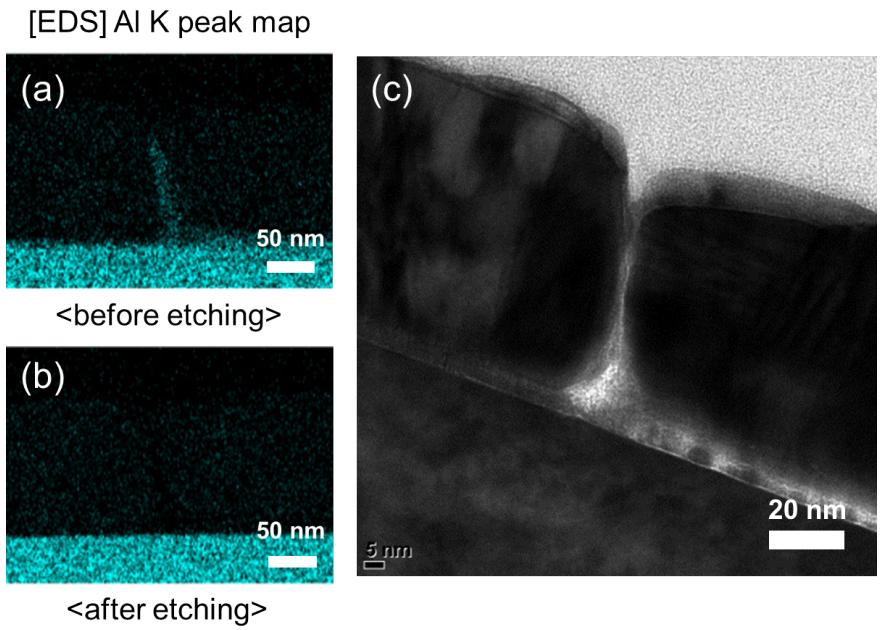

Figure 5.2: Energy dispersive spectroscopy (EDS) image of a 5 nm gap (a) before and (b) after etching, taken with a transmission electron microscope (TEM). The absence of Al peak in the gap confirms the full etching of the alumina spacer. (c) A TEM image of the gap after etching, showing that the gap did not collapse after the wet etching process.

where S, A and L denote solid, air and liquid, respectively, and γ is surface tension at each interface. The parameter should be positive for complete wetting of the solid surface, and when it's negative then surface wets partially. If the surface is wettable then capillary force will bring the water molecules into the gap. For a water-air-metal interfaces, surface tension at liquid-air and liquid-solid interface is too strong (contact angle 130 degrees), giving negative spreading parameter. In a process of wet etching a dielectric, in contrast, the system is now a set of etchant-dielectric-metal interfaces, and surface tension between etchant-dielectric is now negative. The spreading parameter accordingly becomes positive, allowing etchant molecules to enter deep into the gap. Therefore, with careful handling of sample during etching, rinsing and drying process, a spacer-filled nanogap can be fully etched and can retain its high width-to-height ratio without collapsing.

The change in dielectric environment inside the gap leads to spectral changes in transmission and reflection of the gap. When the gap is small enough to be under influence of a gap plasmon, the change is much more dramatic. Since gap plasmon is essentially a coupling of a gap mode with surface mode of the metal-dielectric interface, the effective permittivity of the gap contains both real and imaginary part (Figure 5.3. By etching the gap therefore both amplitude and frequency of the nanogap resonance is expected to change. Figure 5.4 shows transmission spectra of rectangular ring-shaped nanogaps with widths 5, 10 and 20 nm extending over perimeters of 100 um, before and after etching process. Both experiments and calculations show similar trends of resonance blue-shift and increased transmis-

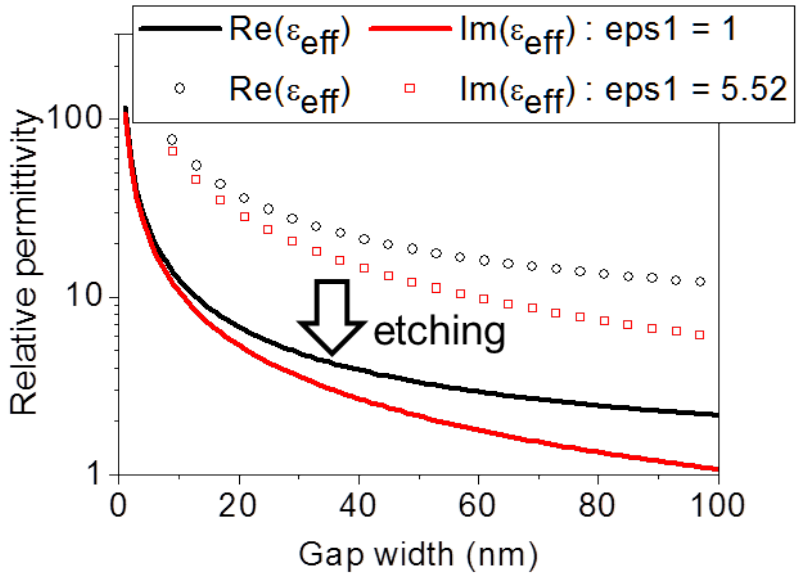

Figure 5.3: Changes in the gap effective permittivity due to etching a gap material (aluminum oxide). Both real and imaginary parts are present even with the lossless gap material.

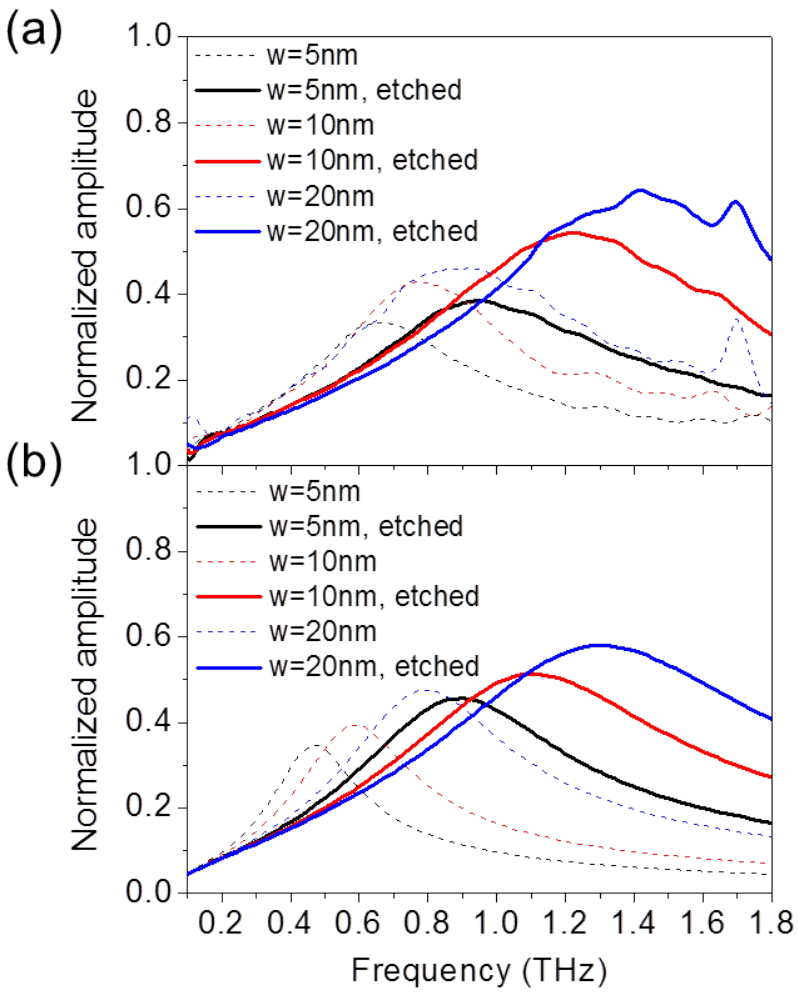

Figure 5.4: (a) Experimentally and (b) theoretically determined terahertz transmission spectrum of 5, 10 and 20 nm-wide nanogap samples before and after etching. Both experiment and theory show increase in resonance frequency and amplitude upon etching the gap.

sion upon etching the gap. It can be inferred from the spectra that the gap did not collapse after the etching process, since otherwise the transmission would have shown a significant decrease in the transmitted amplitude. It is also worth pointing out that the modal expansion-based analytic calculation used in the experiment reproduces the experimental results quite accurately while taking less than 10 minutes for a single structure, while it would have costed several months to simulate the same structure with conventional electromagnetic simulation tools such as finite difference time domain (FDTD) method.

5.3 Liquid water inside nanogaps

Provided that wet etching of a spacer inside the gap is possible, it should be also possible to realize a water-filled gap by exchanging the etchant with water. Figure 5.5 briefly shows the schematic. By diluting the etchant after the whole wet etching process, the gap is slowly filled with water molecules without air molecules having chance to enter the gap. The water-filled nanogaps will show significant decrease in transmitted amplitudes due to enhanced absorption of THz waves by water molecules inside the gap.

Figure 5.6 shows transmission spectra of nanogaps coupled with water, either inside or outside the gap. For comparison, unetched nanogaps coupled with water on top are also measured. Compared to the case where water resides only on top of the gap, the transmission shows significant amplitude decrease and resonance redshift upon filling the gap with water. This is a characteristic response of a slot filled with lossy dielectrics, where real part

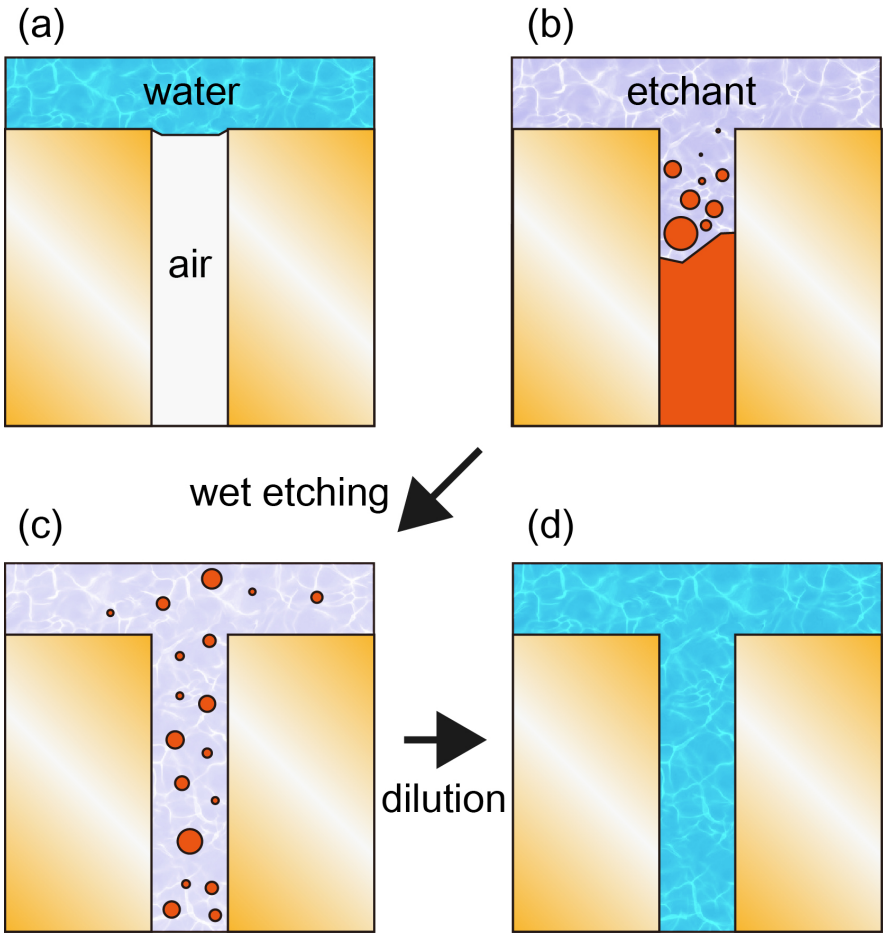

Figure 5.5: Schematics describing the gap etching and filling process. (a) Wetting an air-filled gap is difficult. (b) Wet etching, and (c) subsequent dilution can lead to (d) sub-10 nm gaps filled with water.

of refractive index is responsible for the peak shift and imaginary part for the amplitude decrease. The amplitude decrease can be directly converted into absorption enhancement factor using the Beer-Lambert law[43]:

$$\frac{I}{I_0} = e^{\alpha_{eff} d} \tag{5.2}$$

Here I and I0 is transmitted intensity of sample and reference, respectively, and d is the thickness of the sample. The absorption enhancement factor F can be defined as $\alpha_{eff} = \alpha_0 F$ where α_0 is absorption coefficient of the dielectric without the slot. For the case of nanogaps under influence of gap plasmons, however, changes in the real part also induces an amplitude decrease. The absorption enhancement should therefore be determined solely by the effect from the imaginary part of the refractive index. Since real parts of refractive indices of the spacer ($n_{Al2O3} = 2.35$) and liquid water ($n_{water} = 2.3 + 0.6i$ @1 THz) are similar, the transmission before etching can be a reference for the effect of absorption by water. With the nanogap thickness of 160 nm, the observed 61 percent decrease in transmitted amplitude corresponds to effective absorption coefficient of $\alpha_{eff} = 1.19 \times 10^5 cm^{-1}$, that is, an absorption enhancement factor of F= 700.

The above experiments demonstrate that by appropriate exchanging procedure, spacer material of a sub-10 nm gap can be substituted to various molecules. As a simple demonstration of the concept, an aqueous surface enhanced Raman spectroscopy (SERS) is performed (Figure 5.7). A 10 nm gap is wet etched and filled with water, then subsequently put in contact with 1 mM solution of Rhodamine 6G (R6G). The R6G molecules are

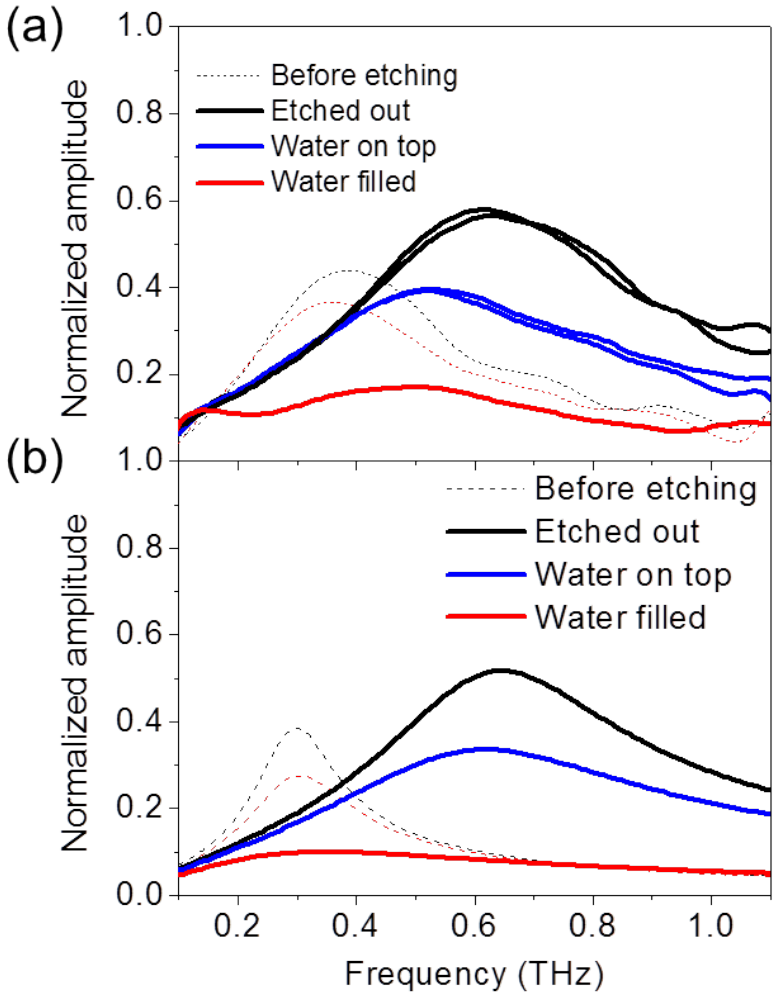

Figure 5.6: (a) Experimentally and (b) theoretically determined terahertz transmission spectra of a 10 nm gap coupled with water. Filling water inside the gap induces much larger amplitude decrease compared to placing water on top of the sample, as well as an additional red-shift in resonance frequency.

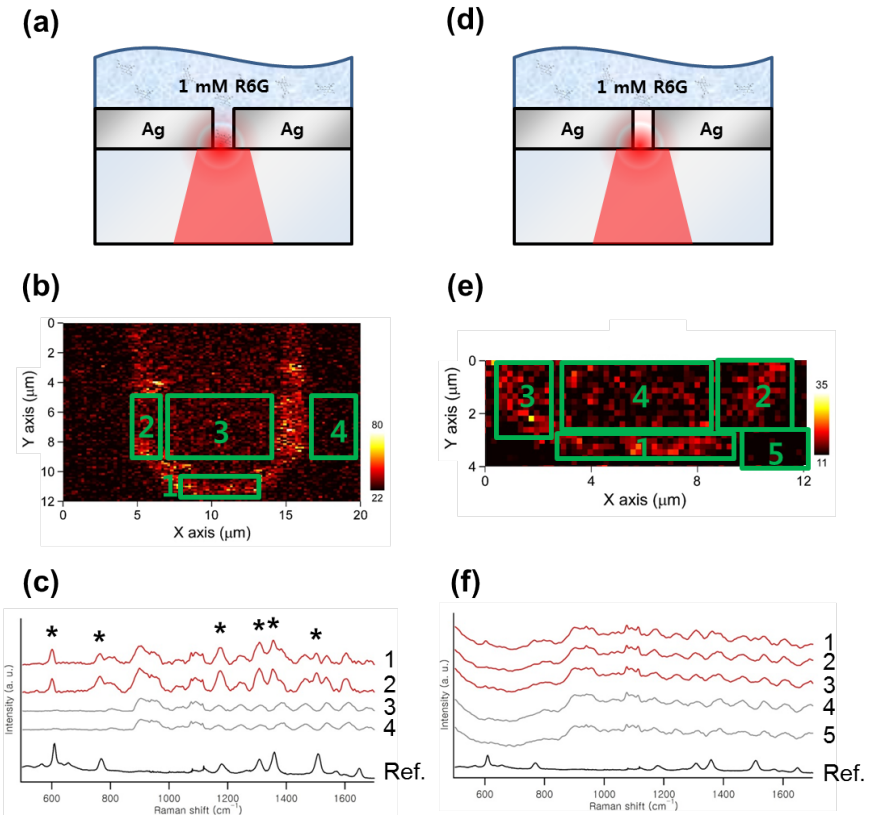

Figure 5.7: (a,d) Gap-enhanced Raman spectroscopy using a water-filled gap and an air-filled gap. (b,e) Scanning Raman image of the gap. (c,f) Raman spectrum of several selected regions. The water-filled gap show scattering peaks from R6G molecules, while the air-filled gap only shows shifts in background level.

about 2 3 nm in size, being able to enter the gap through diffusion. Then the whole sample is illuminated with 633 nm laser from the substrate side, such that Raman scattering could be observed only from molecules inside the gap. The SERS signal show clear sign of R6G at the gap region, and no SERS peaks at the metallic parts. In contrast, if we prepare an etched-out, air-filled nanogap sample and then drop R6G solution on top, no signal of Raman scattering from the R6G molecules can be observed since water cannot fill an air-filled 10 nm metallic gap. This again confirms that water can successfully fill the 10 nm gap with etching and diluting process, and that the procedure is also capable of coupling other molecules with the gap.

Chapter 6

Conclusions and outlook

In this work, we have investigated various aspects of terahertz nano-slots with sub-30 nm widths. Reducing the width of a nano-gap has always been important in the context of better field enhancement and confinement, yet the 10 nm regime is especially important since it is a characteristic length for biomolecules and emergence of quantum effects. For terahertz nano-optics, this is also a regime where noble metals can no more be considered as perfect electric conductors. We have addressed such regime in a comprehensive way throughout this work. We first proposed a spacer-based fabrication method for such terahertz nano-gaps arrays with high throughput and uniformity. Then we investigate the real metal-like effect of the terahertz nanogaps, which we attribute to gap plasmon modes inside the gap. This gives rise to a dramatic resonance red shift and transmission decrease upon narrowing the gap, as well as an anomalously large ohmic absorption of the gap. Lastly, we show that the spacer can be replaced with other systems including air, liquid water and other molecules such as a dye, and observed terahertz absorption enhancement by molecules and Raman scattering exclusively from the gap region. From this study many interesting works are expected, some of which will be presented in the outlook section below.

6.1 Extending outside noble metals

The most important advance in the fabrication method proposed in this work, with respect to the first reported method by Chen et al. [16], is the alleviation of requirements addressing the adhesion of the metal layer. In the previous method where excess metal layer had to be removed by mechanical exfoliation, the metal patterns should not only have vertical sidewalls, but also need to have weak adhesion to dielectric spacer used as a gap material. This limits the use of metals to noble metals such as gold, silver, and copper. By chemical etching of the sacrificial layer for the removal of the excess metal on top, other sticky metals such as chromium, nickel, titanium and iron can be used as the metallic parts of the gap, thereby greatly extending the applicability of the gap. W. Park et al. reported a sub-10 nm chromium nanogap arrays successfully functioning as a lithographic mask, utilizing the high permittivity of chromium at ultraviolet wavelengths [87], using a more sophisticated version of the fabrication to overcome the milling issue associated with chromium. Similar approaches can be made with other types of metals, as many sticky metals have interesting magnetic or superconducting properties which might be useful in future nano-optic applications.

6.2 Detection of nano-confined water

There have been many researches addressing the physical properties of nano-confined water, which shows completely different behavior compared to its bulk counterpart [88, 89, 90, 91, 92]. Most of the reports utilize shear force detection method with atomic force microscope tips to determine

stress tensor of the nanowater [93]. Optical investigation of the nanowater is mostly done in infrared frequencies, where the water absorption is the strongest, and is realized in a very limited set of systems including cryogenic metallic surfaces [94], nanocrystals [95] and aerosols [77]. Much more comprehensive study will be possible with the scheme introduced in this work, since nanogaps can provide a dramatic increase in absorption cross section of the nanoconfined water via field enhancement, and in arbitrary wavelengths via tuning of the gap parameter. Thickness of water can also be controlled as precisely as the spacer deposition can get, which is order of 1 nm for atomic layer deposition and lower for chemical vapor deposition. The interfacing material can also be chosen freely among many metals since the gap can be fabricated in principle with any desired metal as mentioned in the previous section.

Provided that water is successfully coupled with the gap, optical properties of the nano-water can be extracted from the resonant transmission data. Upon filling a waveguide with a lossy dielectric, the resonance frequency of the waveguide will be modified by a factor of real part of refractive index of the dielectric, while the transmitted amplitude will vary according to imaginary part of the refractive index. In case of the nanogap structure proposed in this work, the situation is more complex since real part of refractive index of the gap material also causes transmission decrease when gap plasmon effect is present. Yet the imaginary part of the refractive index induces significant amplitude decrease but negligible resonance shift. The complex refractive index of the gap can therefore be uniquely determined, provided that dispersion of the gap material is negligible.

6.3 Nanogaps as a chemistry platform

Metallic nano-gaps can be considered as a set of well-defined, parallel plate-type electrodes provided that electrolytes fill the gap. The sub-10 nm gaps are especially important in electrochemical applications since molecules behave differently near the electrodes. The qualitatively different layer of molecules near the electrode is called an electric double layer (EDL) and is approximately 2 nm thick in moderate electrolytes [96]. Since EDL is where actual charge transfer takes place in an electrochemical reaction, it is very important to understand the molecular dynamics within the EDL. The effect of EDL becomes even more dominant in nanoporous electrodes, where surface area is maximized by pores with sizes below 10 nm. Yet due to randomness and complex networking of the pores, the nanoporous electrodes are not well suited for systematic study of the EDL. While there have been a number of attempts to fabricate pairs of electrodes seperated by nanometer distances, by far the only possible method to reach sub-10 nm was to utilize a scanning tunneling microscope tip [97]. For parallel plate configuration, the minimum achievable separation is in the order of several tens of nanometers [98, 99]. This work has shown that the limit for parallel plate electrodes can be pushed down to sub-10 nm, enabling a direct access to the EDL layer via C-V measurements and optical characterization.

Also, as mentioned in Chapter 4.2, an intense optical electric field reaching up to 10 V/nm can be realized within the nanogap structure introduced here. Such large electric field can be used to trigger chemical reactions via electron field emission [100], which is capable of inducing nitrogen

plasma [101], polymerization of resist molecules, and redox reactions. The high electric field is also capable of creating a completely new path for a chemical reaction by altering the energy path. One recent theoretical study proposed a path for synthesizing methane and formaldehyde from methanol under 6 V/nm electric field applied [102]. Here the authors proposed to use a tip for applying the high electric field, which is expected to suffer from the small reaction volume near the tip. Our nanoslot structure can be made in wafer scale and in an extended gap geometry, greatly improving the production yield of the proposed chemical reaction. The reaction products can also be detected in real time, using optical spectroscopy techniques such as infrared absorption spectroscopy or Raman scattering spectroscopy.

참고 문헌

[1] M. Brucherseifer, M. Nagel, P. H. Bolivar, H. Kurz, A. Bosserhoff, and R. Buttner, "Label-free probing of the binding state of dna by time-domain terahertz sensing," *Applied Physics Letters*, vol. 77, no. 24, pp. 4049–4051, 2000.

[2] P. C. Upadhya, Y. C. Shen, A. G. Davies, and E. H. Linfield, "Terahertz time-domain spectroscopy of glucose and uric acid," *Journal of Biological Physics*, vol. 29, no. 2-3, pp. 117–121, 2003.

[3] M. Walther, P. Plochocka, B. Fischer, H. Helm, and P. U. Jepsen, "Collective vibrational modes in biological molecules investigated by terahertz time-domain spectroscopy," *Biopolymers*, vol. 67, no. 4-5, pp. 310–313, 2002.

[4] J. Cerne, J. Kono, M. S. Sherwin, M. Sundaram, A. C. Gossard, and G. E. W. Bauer, "Terahertz dynamics of excitons in gaas/algaas quantum wells," *Physical Review Letters*, vol. 77, no. 6, pp. 1131–1134, 1996.

[5] S. Savel'ev, V. A. Yampol'skii, A. L. Rakhmanov, and F. Nori, "Terahertz josephson plasma waves in layered superconductors: spectrum, generation, nonlinear and quantum phenomena," *Reports on Progress in Physics*, vol. 73, no. 2, 2010.

[6] T. Kondo, M. Tonouchi, and M. Hangyo, "Terahertz radiation from superconducting yba2cu3o7-delta thin films with 1.55 mu m excitation," *Japanese Journal of Applied Physics Part 1-Regular Papers Short Notes Review Papers*, vol. 40, no. 2A, pp. 640–643, 2001.

[7] M. Hangyo, S. Tomozawa, Y. Murakami, M. Tonouchi, M. Tani, Z. Wang, K. Sakai, and S. Nakashima, "Terahertz radiation from superconducting yba2cu3o7-delta thin films excited by femtosecond

optical pulses," *Applied Physics Letters*, vol. 69, no. 14, pp. 2122–2124, 1996.

[8] E. Pickwell and V. P. Wallace, "Biomedical applications of terahertz technology," *Journal of Physics D-Applied Physics*, vol. 39, no. 17, pp. R301–R310, 2006.

[9] X. Yang, X. Zhao, K. Yang, Y. P. Liu, Y. Liu, W. L. Fu, and Y. Luo, "Biomedical applications of terahertz spectroscopy and imaging," *Trends in Biotechnology*, vol. 34, no. 10, pp. 810–824, 2016.

[10] D. Zimdars, J. S. White, G. Stuk, A. Chernovsky, G. Fichter, and S. Williamson, "Large area terahertz imaging and non-destructive evaluation applications," *Insight*, vol. 48, no. 9, pp. 537–539, 2006.

[11] I. Amenabar, F. Lopez, and A. Mendikute, "In introductory review to thz non-destructive testing of composite mater," *Journal of Infrared Millimeter and Terahertz Waves*, vol. 34, no. 2, pp. 152–169, 2013.

[12] P. B. Johnson and R. W. Christy, "Optical constants of the noble metals," *Physical Review B*, vol. 6, no. 12, pp. 4370–4379, 1972.

[13] M. A. Ordal, R. J. Bell, R. W. Alexander, L. L. Long, and M. R. Querry, "Optical-properties of 14 metals in the infrared and far infrared - al, co, cu, au, fe, pb, mo, ni, pd, pt, ag, ti, v, and w," *Applied Optics*, vol. 24, no. 24, pp. 4493–4499, 1985.

[14] Y. M. Bahk, H. R. Park, K. J. Ahn, H. S. Kim, Y. H. Ahn, D. S. Kim, J. Bravo-Abad, L. Martin-Moreno, and F. J. Garcia-Vidal, "Anomalous band formation in arrays of terahertz nanoresonators," *Physical Review Letters*, vol. 106, no. 1, 2011.

[15] J. W. Lee, M. A. Seo, D. H. Kang, K. S. Khim, S. C. Jeoung, and D. S. Kim, "Terahertz electromagnetic wave transmission through random arrays of single rectangular holes and slits in thin metallic sheets," *Physical Review Letters*, vol. 99, no. 13, 2007.

[16] X. S. Chen, H. R. Park, M. Pelton, X. J. Piao, N. C. Lindquist, H. Im, Y. J. Kim, J. S. Ahn, K. J. Ahn, N. Park, D. S. Kim, and S. H. Oh, "Atomic layer lithography of wafer-scale nanogap arrays for extreme confinement of electromagnetic waves," *Nature Communications*, vol. 4, 2013.

[17] S. Kumar, "Recent progress in terahertz quantum cascade lasers," *Ieee Journal of Selected Topics in Quantum Electronics*, vol. 17, no. 1, pp. 38–47, 2011.

[18] B. S. Williams, "Terahertz quantum-cascade lasers," *Nature Photonics*, vol. 1, no. 9, pp. 517–525, 2007.

[19] N. Vinokurov, "Free electron lasers as a high-power terahertz sources," *Journal of Infrared Millimeter and Terahertz Waves*, vol. 32, no. 10, pp. 1123–1143, 2011.

[20] B. A. Knyazev, G. N. Kulipanov, and N. A. Vinokurov, "Novosibirsk terahertz free electron laser: instrumentation development and experimental achievements," *Measurement Science and Technology*, vol. 21, no. 5, 2010.

[21] J. M. Byrd, W. P. Leemans, A. Loftsdottir, B. Marcelis, M. C. Martin, W. R. McKinney, F. Sannibale, T. Scarvie, and C. Steier, "Observation of broadband self-amplified spontaneous coherent terahertz synchrotron radiation in a storage ring," *Physical Review Letters*, vol. 89, no. 22, 2002.

[22] H. W. Hubers, A. Semenov, K. Holldack, U. Schade, G. Wustefeld, and G. Gol'tsman, "Time domain analysis of coherent terahertz synchrotron radiation," *Applied Physics Letters*, vol. 87, no. 18, 2005.

[23] M. Tonouchi, "Cutting-edge terahertz technology," *Nature Photonics*, vol. 1, no. 2, pp. 97–105, 2007.

[24] B. Ferguson and X. C. Zhang, "Materials for terahertz science and technology," *Nature Materials*, vol. 1, no. 1, pp. 26–33, 2002.

[25] P. U. Jepsen, R. H. Jacobsen, and S. R. Keiding, "Generation and detection of terahertz pulses from biased semiconductor antennas," *Journal of the Optical Society of America B-Optical Physics*, vol. 13, no. 11, pp. 2424–2436, 1996.

[26] H. Hirori, A. Doi, F. Blanchard, and K. Tanaka, "Single-cycle terahertz pulses with amplitudes exceeding 1 mv/cm generated by optical rectification in linbo3," *Applied Physics Letters*, vol. 98, no. 9, 2011.

[27] K. L. Yeh, M. C. Hoffmann, J. Hebling, and K. A. Nelson, "Generation of 10 mu j ultrashort terahertz pulses by optical rectification," *Applied Physics Letters*, vol. 90, no. 17, 2007.

[28] A. Leitenstorfer, S. Hunsche, J. Shah, M. C. Nuss, and W. H. Knox, "Detectors and sources for ultrabroadband electro-optic sampling: Experiment and theory," *Applied Physics Letters*, vol. 74, no. 11, pp. 1516–1518, 1999.

[29] A. Nahata, A. S. Weling, and T. F. Heinz, "A wideband coherent terahertz spectroscopy system using optical rectification and electro-optic sampling," *Applied Physics Letters*, vol. 69, no. 16, pp. 2321–2323, 1996.

[30] M. Shalaby, H. Merbold, M. Peccianti, L. Razzari, G. Sharma, T. Ozaki, R. Morandotti, T. Feurer, A. Weber, L. Heyderman, B. Patterson, and H. Sigg, "Concurrent field enhancement and high transmission of thz radiation in nanoslit arrays," *Applied Physics Letters*, vol. 99, no. 4, 2011.

[31] M. A. Seo, H. R. Park, S. M. Koo, D. J. Park, J. H. Kang, O. K. Suwal, S. S. Choi, P. C. M. Planken, G. S. Park, N. K. Park, Q. H. Park, and D. S. Kim, "Terahertz field enhancement by a metallic nano slit operating beyond the skin-depth limit," *Nature Photonics*, vol. 3, no. 3, pp. 152–156, 2009.

[32] K. Yoshida, K. Shibata, and K. Hirakawa, "Terahertz field enhancement and photon-assisted tunneling in single-molecule transistors," *Physical Review Letters*, vol. 115, no. 13, 2015.

[33] K. Ishihara, K. Ohashi, T. Ikari, H. Minamide, H. Yokoyama, J. Shikata, and H. Ito, "Terahertz-wave near-field imaging with subwavelength resolution using surface-wave-assisted bow-tie aperture," *Applied Physics Letters*, vol. 89, no. 20, 2006.

[34] S. Mastel, M. B. Lundeberg, P. Alonso-González, Y. Gao, K. Watanabe, T. Taniguchi, J. Hone, F. H. L. Koppens, A. Y. Nikitin, and R. Hillenbrand, "Terahertz nanofocusing with cantilevered terahertz-resonant antenna tips," *Nano Letters*, vol. 17, no. 11, pp. 6526–6533, 2017.

[35] H. T. Chen, R. Kersting, and G. C. Cho, "Terahertz imaging with nanometer resolution," *Applied Physics Letters*, vol. 83, no. 15, pp. 3009–3011, 2003.

[36] D. J. Park, S. B. Choi, Y. H. Ahn, F. Rotermund, I. B. Sohn, C. Kang, M. S. Jeong, and D. S. Kim, "Terahertz near-field enhancement in narrow rectangular apertures on metal film," *Optics Express*, vol. 17, no. 15, pp. 12493–12501, 2009.

[37] H. R. Park, Y. M. Park, H. S. Kim, J. S. Kyoung, M. A. Seo, D. J. Park, Y. H. Ahn, K. J. Ahn, and D. S. Kim, "Terahertz nanoresonators: Giant field enhancement and ultrabroadband performance," *Applied Physics Letters*, vol. 96, no. 12, 2010.

[38] H. R. Park, S. M. Koo, O. K. Suwal, Y. M. Park, J. S. Kyoung, M. A. Seo, S. S. Choi, N. K. Park, D. S. Kim, and K. J. Ahn, "Resonance behavior of single ultrathin slot antennas on finite dielectric substrates in terahertz regime," *Applied Physics Letters*, vol. 96, no. 21, 2010.

[39] Y. M. Bahk, J. W. Choi, J. Kyoung, H. R. Park, K. J. Ahn, and D. S. Kim, "Selective enhanced resonances of two asymmetric terahertz

nano resonators," *Optics Express*, vol. 20, no. 23, pp. 25644–25653, 2012.

[40] S. B. Choi, J. S. Kyoung, H. S. Kim, H. R. Park, D. J. Park, B. J. Kim, Y. H. Ahn, F. Rotermund, H. T. Kim, K. J. Ahn, and D. S. Kim, "Nanopattern enabled terahertz all-optical switching on vanadium dioxide thin film," *Applied Physics Letters*, vol. 98, no. 7, 2011.

[41] Y. G. Jeong, H. Bernien, J. S. Kyoung, H. R. Park, H. S. Kim, J. W. Choi, B. J. Kim, H. T. Kim, K. J. Ahn, and D. S. Kim, "Electrical control of terahertz nano antennas on vo2 thin film," *Optics Express*, vol. 19, no. 22, pp. 21211–21215, 2011.

[42] Y. G. Jeong, S. Han, J. Rhie, J. S. Kyoung, J. W. Choi, N. Park, S. Hong, B. J. Kim, H. T. Kim, and D. S. Kim, "A vanadium dioxide metamaterial disengaged from insulator-tometal transition," *Nano Letters*, vol. 15, no. 10, pp. 6318–6323, 2015.

[43] H. R. Park, K. J. Ahn, S. Han, Y. M. Bahk, N. Park, and D. S. Kim, "Colossal absorption of molecules inside single terahertz nanoantennas," *Nano Letters*, vol. 13, no. 4, pp. 1782–1786, 2013.

[44] D. K. Lee, J. H. Kang, J. S. Lee, H. S. Kim, C. Kim, J. H. Kim, T. Lee, J. H. Son, Q. H. Park, and M. Seo, "Highly sensitive and selective sugar detection by terahertz nano-antennas," *Scientific Reports*, vol. 5, 2015.

[45] H. R. Park, Y. M. Bahk, K. J. Ahn, Q. H. Park, D. S. Kim, L. Martin-Moreno, F. J. Garcia-Vidal, and J. Bravo-Abad, "Controlling terahertz radiation with nanoscale metal barriers embedded in nano slot antennas," *Acs Nano*, vol. 5, no. 10, pp. 8340–8345, 2011.

[46] H. R. Park, Y. M. Bahk, J. H. Choe, S. Han, S. S. Choi, K. J. Ahn, N. Park, Q. H. Park, and D. S. Kim, "Terahertz pinch harmonics enabled by single nano rods," *Optics Express*, vol. 19, no. 24, pp. 24775–24781, 2011.

[47] G. Choi, Y.-M. Bahk, T. Kang, Y. Lee, B. H. Son, Y. H. Ahn, M. Seo, and D.-S. Kim, "Terahertz nanoprobing of semiconductor surface dynamics," *Nano Letters*, vol. 17, no. 10, pp. 6397–6401, 2017. PMID: 28945438.

[48] J. S. Kyoung, M. A. Seo, H. R. Park, K. J. Ahn, and D. S. Kim, "Far field detection of terahertz near field enhancement of sub-wavelength slits using kirchhoff integral formalism," *Optics Communications*, vol. 283, no. 24, pp. 4907–4910, 2010.

[49] S. A. Maier, *Plasmonics: fundamentals and applications*. Springer Science Business Media, 2007.

[50] M. S. Nezami, D. Yoo, G. Hajisalem, S. H. Oh, and R. Gordon, "Gap plasmon enhanced metasurface third-harmonic generation in transmission geometry," *Acs Photonics*, vol. 3, no. 8, pp. 1461–1467, 2016.

[51] R. Gordon, A. I. K. Choudhury, and T. Lu, "Gap plasmon mode of eccentric coaxial metal waveguide," *Optics Express*, vol. 17, no. 7, pp. 5311–5320, 2009.

[52] Y. C. Jun, R. Pala, and M. L. Brongersma, "Strong modification of quantum dot spontaneous emission via gap plasmon coupling in metal nanoslits," *Journal of Physical Chemistry C*, vol. 114, no. 16, pp. 7269–7273, 2010.

[53] D. F. P. Pile, T. Ogawa, D. K. Gramotnev, Y. Matsuzaki, K. C. Vernon, K. Yamaguchi, T. Okamoto, M. Haraguchi, and M. Fukui, "Two-dimensionally localized modes of a nanoscale gap plasmon waveguide," *Applied Physics Letters*, vol. 87, no. 26, 2005.

[54] L. F. Sun, S. N. Chin, E. Marx, K. S. Curtis, N. C. Greenham, and C. J. B. Ford, "Shadow-evaporated nanometre-sized gaps and their use in electrical studies of nanocrystals," *Nanotechnology*, vol. 16, no. 6, pp. 631–634, 2005.

[55] G. Philipp, T. Weimann, P. Hinze, M. Burghard, and J. Weis, "Shadow evaporation method for fabrication of sub 10 nm gaps between metal electrodes," *Microelectronic Engineering*, vol. 46, no. 1-4, pp. 157–160, 1999.

[56] S. M. George, "Atomic layer deposition: An overview," *Chemical Reviews*, vol. 110, no. 1, pp. 111–131, 2010.

[57] J. Jeong, J. Rhie, W. Jeon, C. S. Hwang, and D. S. Kim, "High-throughput fabrication of infinitely long 10 nm slit arrays for terahertz applications," *Journal of Infrared Millimeter and Terahertz Waves*, vol. 36, no. 3, pp. 262–268, 2015.

[58] F. J. Garcia-Vidal, E. Moreno, J. A. Porto, and L. Martin-Moreno, "Transmission of light through a single rectangular hole," *Physical Review Letters*, vol. 95, no. 10, 2005.

[59] F. J. Garcia-Vidal, L. Martin-Moreno, E. Moreno, L. K. S. Kumar, and R. Gordon, "Transmission of light through a single rectangular hole in a real metal," *Physical Review B*, vol. 74, no. 15, 2006.

[60] R. Budwig, "Refractive-index matching methods for liquid flow investigations," *Experiments in Fluids*, vol. 17, no. 5, pp. 350–355, 1994.

[61] X. Yan, D. J. Poxson, J. Cho, R. E. Welser, A. K. Sood, J. K. Kim, and E. F. Schubert, "Enhanced omnidirectional photovoltaic performance of solar cells using multiple-discrete-layer tailored- and low-refractive index anti-reflection coatings," *Advanced Functional Materials*, vol. 23, no. 5, pp. 583–590, 2013.

[62] T. Trupke, A. Shalav, B. S. Richards, P. Wurfel, and M. A. Green, "Efficiency enhancement of solar cells by luminescent up-conversion of sunlight," *Solar Energy Materials and Solar Cells*, vol. 90, no. 18-19, pp. 3327–3338, 2006.

[63] J. D. Jackson, *Classical electrodynamics*. AAPT, 1999.

[64] H. W. Kihm, S. M. Koo, Q. H. Kim, K. Bao, J. E. Kihm, W. S. Bak, S. H. Eah, C. Lienau, H. Kim, P. Nordlander, N. J. Halas, N. K. Park, and D. S. Kim, "Bethe-hole polarization analyser for the magnetic vector of light," *Nature Communications*, vol. 2, 2011.

[65] D. Lee and D. S. Kim, "Light scattering of rectangular slot antennas: parallel magnetic vector vs perpendicular electric vector," *Scientific Reports*, vol. 6, 2016.

[66] Y. M. Bahk, B. J. Kang, Y. S. Kim, J. Y. Kim, W. T. Kim, T. Y. Kim, T. Kang, J. Rhie, S. Han, C. H. Park, F. Rotermund, and D. S. Kim, "Electromagnetic saturation of angstrom-sized quantum barriers at terahertz frequencies," *Physical Review Letters*, vol. 115, no. 12, 2015.

[67] J. Y. Kim, B. J. Kang, J. Park, Y. M. Bahk, W. T. Kim, J. Rhie, H. Jeon, F. Rotermund, and D. S. Kim, "Terahertz quantum plasmonics of nanoslot antennas in nonlinear regime," *Nano Letters*, vol. 15, no. 10, pp. 6683–6688, 2015.

[68] C. M. Watts, X. L. Liu, and W. J. Padilla, "Metamaterial electromagnetic wave absorbers," *Advanced Materials*, vol. 24, no. 23, pp. Op98–Op120, 2012.

[69] H. Tao, C. M. Bingham, D. Pilon, K. B. Fan, A. C. Strikwerda, D. Shrekenhamer, W. J. Padilla, X. Zhang, and R. D. Averitt, "A dual band terahertz metamaterial absorber," *Journal of Physics D-Applied Physics*, vol. 43, no. 22, 2010.

[70] H. T. Chen, J. F. O'Hara, A. K. Azad, A. J. Taylor, R. D. Averitt, D. B. Shrekenhamer, and W. J. Padilla, "Experimental demonstration of frequency-agile terahertz metamaterials," *Nature Photonics*, vol. 2, no. 5, pp. 295–298, 2008.

[71] D. H. Choi, H. Son, S. Jung, J. Park, W. Y. Park, O. S. Kwon, and G. S. Park, "Dielectric relaxation change of water upon phase transi-

tion of a lipid bilayer probed by terahertz time domain spectroscopy," *Journal of Chemical Physics*, vol. 137, no. 17, 2012.

[72] M. Falk, A. Poole, and C. Goymour, "Infrared study of the state of water in the hydration shell of dna," *Canadian Journal of Chemistry*, vol. 48, no. 10, pp. 1536–1542, 1970.

[73] E. Liepinsh, G. Otting, and K. Wuthrich, "Nmr observation of individual molecules of hydration water bound to dna duplexes - direct evidence for a spine of hydration water present in aqueous-solution," *Nucleic Acids Research*, vol. 20, no. 24, pp. 6549–6553, 1992.

[74] S. J. Kim, B. Born, M. Havenith, and M. Gruebele, "Real-time detection of protein-water dynamics upon protein folding by terahertz absorption spectroscopy," *Angewandte Chemie-International Edition*, vol. 47, no. 34, pp. 6486–6489, 2008.

[75] J. Q. Zhang and D. Grischkowsky, "Waveguide terahertz time-domain spectroscopy of nanometer water layers," *Optics Letters*, vol. 29, no. 14, pp. 1617–1619, 2004.

[76] A. Verdaguer, G. M. Sacha, H. Bluhm, and M. Salmeron, "Molecular structure of water at interfaces: Wetting at the nanometer scale," *Chemical Reviews*, vol. 106, no. 4, pp. 1478–1510, 2006.

[77] J. Q. Zhang and D. Grischkowsky, "Terahertz time-domain spectroscopy of submonolayer water adsorption in hydrophilic silica aerogel," *Optics Letters*, vol. 29, no. 9, pp. 1031–1033, 2004.

[78] F. Yavari, C. Kritzinger, C. Gaire, L. Song, H. Gullapalli, T. Borca-Tasciuc, P. M. Ajayan, and N. Koratkar, "Tunable bandgap in graphene by the controlled adsorption of water molecules," *Small*, vol. 6, no. 22, pp. 2535–2538, 2010.

[79] T. A. Ho and A. Striolo, "Polarizability effects in molecular dynamics simulations of the graphene-water interface," *Journal of Chemical Physics*, vol. 138, no. 5, 2013.

[80] B. Corry, "Designing carbon nanotube membranes for efficient water desalination," *Journal of Physical Chemistry B*, vol. 112, no. 5, pp. 1427–1434, 2008.

[81] D. Cohen-Tanugi and J. C. Grossman, "Water desalination across nanoporous graphene," *Nano Letters*, vol. 12, no. 7, pp. 3602–3608, 2012.

[82] J. Rossmeisl, Z. W. Qu, H. Zhu, G. J. Kroes, and J. K. Norskov, "Electrolysis of water on oxide surfaces," *Journal of Electroanalytical Chemistry*, vol. 607, no. 1-2, pp. 83–89, 2007.

[83] K. Zeng and D. K. Zhang, "Recent progress in alkaline water electrolysis for hydrogen production and applications," *Progress in Energy and Combustion Science*, vol. 36, no. 3, pp. 307–326, 2010.

[84] L. Thrane, R. H. Jacobsen, P. U. Jepsen, and S. R. Keiding, "Thz reflection spectroscopy of liquid water," *Chemical Physics Letters*, vol. 240, no. 4, pp. 330–333, 1995.

[85] M. Heyden, J. Sun, S. Funkner, G. Mathias, H. Forbert, M. Havenith, and D. Marx, "Dissecting the thz spectrum of liquid water from first principles via correlations in time and space," *Proceedings of the National Academy of Sciences of the United States of America*, vol. 107, no. 27, pp. 12068–12073, 2010.

[86] H. Yada, M. Nagai, and K. Tanaka, "Origin of the fast relaxation component of water and heavy water revealed by terahertz time-domain attenuated total reflection spectroscopy," *Chemical Physics Letters*, vol. 464, no. 4-6, pp. 166–170, 2008.

[87] W. Park, J. Rhie, N. Y. Kim, S. Hong, and D. S. Kim, "Sub-10 nm feature chromium photomasks for contact lithography patterning of square metal ring arrays," *Scientific Reports*, vol. 6, 2016.

[88] E. M. Choi, Y. H. Yoon, S. Lee, and H. Kang, "Freezing transition of interfacial water at room temperature under electric fields," *Physical Review Letters*, vol. 95, no. 8, 2005.

[89] S. T. van der Post, C. S. Hsieh, M. Okuno, Y. Nagata, H. J. Bakker, M. Bonn, and J. Hunger, "Strong frequency dependence of vibrational relaxation in bulk and surface water reveals sub-picosecond structural heterogeneity," *Nature Communications*, vol. 6, 2015.

[90] B. Kim, S. Kwon, H. Mun, S. An, and W. Jhe, "Energy dissipation of nanoconfined hydration layer: Long-range hydration on the hydrophilic solid surface," *Scientific Reports*, vol. 4, 2014.

[91] K. Ataka, T. Yotsuyanagi, and M. Osawa, "Potential-dependent reorientation of water molecules at an electrode/electrolyte interface studied by surface-enhanced infrared absorption spectroscopy," *Journal of Physical Chemistry*, vol. 100, no. 25, pp. 10664–10672, 1996.

[92] A. Verdaguer, G. M. Sacha, H. Bluhm, and M. Salmeron, "Molecular structure of water at interfaces: Wetting at the nanometer scale," *Chemical Reviews*, vol. 106, no. 4, pp. 1478–1510, 2006.

[93] M. Lee, B. Kim, J. Kim, and W. Jhe, "Noncontact friction via capillary shear interaction at nanoscale," *Nature Communications*, vol. 6, 2015.

[94] Y. Kim, E. S. Moon, S. Shin, and H. Kang, "Acidic water monolayer on ruthenium(0001)," *Angewandte Chemie-International Edition*, vol. 51, no. 51, pp. 12806–12809, 2012.

[95] E. S. Zhukova, V. I. Torgashev, B. P. Gorshunov, V. V. Lebedev, G. S. Shakurov, R. K. Kremer, E. V. Pestrjakov, V. G. Thomas, D. A. Fursenko, A. S. Prokhorov, and M. Dressel, "Vibrational states of a water molecule in a nano-cavity of beryl crystal lattice," *Journal of Chemical Physics*, vol. 140, no. 22, 2014.

[96] J. H. Bae, J. H. Han, and T. D. Chung, "Electrochemistry at nanoporous interfaces: new opportunity for electrocatalysis," *Physical Chemistry Chemical Physics*, vol. 14, no. 2, pp. 448–463, 2012.

[97] Y. H. Yoon, D. H. Woo, T. Shin, T. D. Chung, and H. Kang, "Real-space investigation of electrical double layers. potential gradient measurement with a nanometer potential probe," *Journal of Physical Chemistry C*, vol. 115, no. 35, pp. 17384–17391, 2011.

[98] M. A. G. Zevenbergen, P. S. Singh, E. D. Goluch, B. L. Wolfrum, and S. G. Lemay, "Stochastic sensing of single molecules in a nanofluidic electrochemical device," *Nano Letters*, vol. 11, no. 7, pp. 2881–2886, 2011.

[99] E. Katelhon, B. Hofmann, S. G. Lemay, M. A. G. Zevenbergen, A. Offenhausser, and B. Wolfrum, "Nanocavity redox cycling sensors for the detection of dopamine fluctuations in microfluidic gradients," *Analytical Chemistry*, vol. 82, no. 20, pp. 8502–8509, 2010.

[100] J. D. Zhang, X. G. Zhao, K. B. Fan, X. N. Wang, G. F. Zhang, K. Geng, X. Zhang, and R. D. Averitt, "Terahertz radiation-induced sub-cycle field electron emission across a split-gap dipole antenna," *Applied Physics Letters*, vol. 107, no. 23, 2015.

[101] K. Iwaszczuk, M. Zalkovskij, A. C. Strikwerda, and P. U. Jepsen, "Nitrogen plasma formation through terahertz-induced ultrafast electron field emission," *Optica*, vol. 2, no. 2, pp. 116–123, 2015.

[102] G. Cassone, F. Pietrucci, F. Saija, F. Guyot, and A. M. Saitta, "One-step electric-field driven methane and formaldehyde synthesis from liquid methanol," *Chemical Science*, vol. 8, no. 3, pp. 2329–2336, 2017.

초 록

본 논문에서는 대부분의 금속이 완전전도체로 근사될 수 있는 테라헤르츠 주파수에서 금속 나노구조의 특성이 불완전전도체의 특성을 보이는 현상에 대해 보고한다. 나노구조의 선폭이 약 100 나노미터 이하로 내려갈 경우 양 옆의 금속 층이 상호작용 하면서 갭 플라즈몬을 생성하는데, 이로 인해 유전율이 10^6 이상인 금속에 상당한 양의 전기장이 스며들 수 있게 된다. 따라서 우선 이와 같은 금속 나노구조를 안정적으로 제작할 수 있는 방법을 제시하고, 이와 같은 구조를 분석하여 공진 주파수와 세기 그리고 60% 이상의 금속 광 흡수를 성공적으로 관찰하고 이론적으로 예측하였다. 또한 유전박막이 차 있는 5 나노미터 너비, 200 나노미터 깊이의 틈을 성공적으로 식각하고 물로 채움으로써 수중 환경에서의 나노광학적 분석을 10 나노미터 이하 스케일에서 가능하게 하였다. 위 연구는 금속 나노구조의 활용에 있어 필요한 내용을 포괄적으로 다루고 있어 차후 광 흡수 메타물질, 광화학 및 생명공학 분야의 응용에 큰 도움이 될 것으로 기대한다.

주요어 : 테라헤르츠 나노갭, 갭 플라즈몬, 광 흡수 메타물질

학번 : 2014-30106